UNIVERSIDADE FEDERAL DE SANTA CATARINA
DEPARTAMENTO DE ENGENHARIA MECÂNICA

Gabriel Silva de Matos

LASER TRIANGULATION SENSOR WITH REFRACTION MODELLING FOR UNDERWATER 3D MEASUREMENT

Florianópolis

2017

Gabriel Silva de Matos

LASER TRIANGULATION SENSOR WITH REFRACTION MODELLING FOR UNDERWATER 3D MEASUREMENT

Dissertação submetida ao Programa de Pós-Graduação em Engenharia Mecânica para a obtenção do Grau de Mestre em Engenharia Mecânica.
Orientador: Tiago Loureiro Figaro da Costa Pinto, Dr. Eng.

Florianópolis

2017

Gabriel Silva de Matos

LASER TRIANGULATION SENSOR WITH REFRACTION MODELLING FOR UNDERWATER 3D MEASUREMENT

Esta Dissertação foi julgada aprovada para a obtenção do Título de "Mestre em Engenharia Mecânica", e aprovada em sua forma final pelo Programa de Pós-Graduação em Engenharia Mecânica.

Florianópolis, 8 de Maio 2017.

Jonny Carlos da Silva, Dr. Eng.
Coordenador

Tiago Loureiro Figaro da Costa Pinto, Dr. Eng.
Orientador

Banca Examinadora:

Tiago Loureiro Figaro da Costa Pinto, Dr. Eng.
Presidente

Armando Albertazzi Gonçalves Júnior, Dr. Eng.

Marcelo Ricardo Stemmer, Dr.-Ing.

Walter Antonio Kapp, Dr. Eng.

Marco Antonio Martins Cavaco, PhD.

ACKNOWLEDGEMENTS

To my parents, Daniel and Anesia, who have always supported me and taught me the importance of education.

To Marcella, my life partner, thank you for all the love, trust and companionship.

To Prof. Tiago Pinto, for believing in my capabilities and for the valuable advice, availability and cooperation throughout this work.

To all the LABMETRO staff for their assistance throughout the progress of this work. Especially, to Pedro for sharing the technical discussions, to Fabio for guidance during the mechanical design and Rosana, who was always ready to help.

To the Brazilian Institute of Oil Gas and Biofuels (IBP), who provided the funding for this work.

And to all my family and friends for accompanying me along this path.

RESUMO

Medições tridimensionais em ambientes subaquáticos são úteis em diversas aplicações. Por exemplo, a indústria de petróleo e gás possui muitos equipamentos utilizados na extração de petróleo que necessitam de manutenção constante, a biologia tem grande interesse em investigar a vida submarina e investigações de naufrágios podem fornecer dados úteis. No entanto, nem sempre é uma tarefa fácil obter dados subaquáticos confiáveis, porque a luz espalha-se, é absorvida e refrata e o som nem sempre pode fornecer uma boa resolução em curtas distâncias. Estes obstáculos devem ser considerados para alcançar os melhores resultados de medição possíveis.

Este trabalho está dividido em quatro partes: uma revisão das técnicas de digitalização 3D subaquáticas disponíveis, o projeto mecânico e óptico do sistema para atender aos objetivos descritos, os algoritmos de calibração e de medição utilizados com o sensor e uma avaliação final com comparações entre o método proposto e um método de referência.

Atualmente, diversos métodos são utilizados para realizar a digitalização destes ambientes, alguns destes são: Sound Navigation and Ranging (sonar) , Light Detection And Ranging (LiDAR), visão estéreo e triangulação laser. O sonar é amplamente utilizado em embarcações marítimas para obter informações sobre a profundidade e o fundo do mar e para a localização e mapeamento simultâneos (SLAM) associados a veículos operados remotamente (ROVs). Mas eles também podem ser usados em medições tridimensionais sendo por vezes chamados como câmeras acústicas. Eles são baseados na emissão de um pulso sonoros e na medição do tempo de vôo do sinal. Sendo eles divididos em único feixe, que fornece informação de azimute e distância; múltiplos feixes, que fornece múltiplos azimutes e distâncias e de feixe lateral, que utiliza uma onda em forma de cone para obter uma imagem acústica. Uma das grandes vantagens dos sonares é a capacidade de obter dados confiáveis mesmo em águas muito turvas. LiDAR também é uma técnica de tempo de vôo, entretanto ele utiliza a luz para obter o tempo de retorno do sinal.

A fotogrametria é uma técnica que utiliza imagens para obter informações como distâncias e geometrias da cena. Exemplos de fotogrametria são a visão estéreo e a triangulação laser. Entretanto, ela possui limitações em ambientes subaquáticos, porque a luz sofre diversas influências da água. Apesar disto, em medições de curta distância,

até 10 m, elas possuem as menores incertezas entre as outras técnicas apresentadas. Uma consideração comum na fotogrametria é a consideração da câmera *pinhole*: todos os raios de luz passam pelo centro de pupila da câmera e projetam-se no plano imagem. Neste modelo a calibração consiste em obter a matriz de projeção da câmera, a matriz que projeta um ponto 3D qualquer em um ponto na imagem.

Técnicas de visão estéreo utilizam duas ou mais câmeras para obter a nuvem de pontos tridimensionais. Nelas a matriz de projeção é utilizada para projetar retas de pontos homólogos, mesmo ponto 3D representado em diferentes imagens. O cruzamento destas retas resulta no ponto 3D medido. Para obter estes pontos homólogos a cena pode ser iluminada com projeção de luz estruturada ou iluminação passiva. Um exemplo de luz estruturada é a projeção de franjas senoidais, possibilitando a assinatura única dos diversos pontos 3D. Assim, a busca de pontos homólogos resume-se em buscar pontos na imagem com o mesmo valor de fase.

A triangulação laser pode ser considerada uma forma de fotogrametria com iluminação estruturada, já que um laser é utilizado para iluminar a cena e uma câmera observa-o com certo ângulo. Os principais parâmetros que definem um sistema de triangulação laser são: o *baseline* (distância entre o centro do *pinhole* da câmera e o eixo do laser), o ângulo de triangulação (ângulo entre o eixo da câmera e o eixo do laser), o foco da lente, o tamanho do pixel da câmera e a resolução da câmera. Dois mêtodos de calibração do sistema são demonstrados. No primeiro, polinômios são ajustados para correlacionar o pico laser detectado com o ponto 3D medido. No segundo, o modelo *pinhole* é utilizado em conjunto com um ajuste matemático do plano laser, tornando, assim, possível traçar uma reta da câmera que cruza com o plano laser ajustado.

Embaixo d'água, a luz sofre diversas alteração quando comparada com seu comportamento no ar. As principais alterações são: absorção, espalhamento e refração. A absorção acontece principalmente nos comprimentos de onda próximos do vermelho (650 nm) . Já o espalhamento tem uma maior influência nos comprimentos de onda azuis (450 nm), resultando na cor dos oceanos. Assim, uma solução de compromisso é necessária, sendo, geralmente, lasers próximos do verde escolhidos para medições em distâncias maiores. A refração resulta em uma "distorção 3D", pois o desvio do raio depende da distância do objeto. Entretanto, conhecendo-se o eixo de refração, as distâncias entre as interfaces de refração e o primeiro raio de projeção da câmera é possível determinar o raio final da refração.

O sistema proposto possui os seguintes objetivos: o sensor deve ser projetado para medir um quinto da secção transversal exterior de um tubo de 300 mm de diâmetro, a incerteza de medição final deve ser próxima de décimos de milímetros, a distância do sistema de medição à superfície de interesse deve ser suficiente para garantir a segurança do equipamento, por fim, o sistema também deve ser modular, para permitir mudanças futuras no volume de medição, com alterações na *baseline* do sistema e no ângulo de triangulação. Após diversos cálculos e simulações o sensor que cumpre estes requisitos tem as seguintes características: *baseline* de 265 mm, ângulo de triangulação de 35°, distância focal da lente de 12.5 mm, resolução do sensor de 1280x1024 pixels e tamanho do pixel de 5.5 µm. Esta configuração garante uma profundidade de medição de 220 mm com uma distância mínima de medição de 200 mm e um comprimento de 180 mm ao longo da linha laser no stand-off. Além do sistema, uma bancada para medição e calibração também foi construída. Ela consiste em uma mesa de deslocamento linear, um tanque para medição, um tanque de armazenamento e de um sistema hidráulico, permitindo, assim, a medição tanto no ar como na água em todo o volume de medição.

Algoritmos de medição e calibração foram desenvolvidos. A medição consiste em traçar o caminho inverso do raio de luz, da câmera até o plano laser. O primeiro passo é obter o raio saindo do pico laser detectado na imagem utilizando a matriz de calibração da câmera. Depois, o cruzamento deste raio com o plano de refração é medido utilizando a distância do centro óptico até a janela de refração. O raio é, então, refratado e o cruzamento deste raio com o plano laser é computado. Para obter a distância do centro óptico até a janela de refração uma calibração é proposta. Nesta calibração, uma aquisição subaquática de um degrau é realizada e a altura do degrau é medida utilizando-se distâncias de janela próximas às do projeto mecânico. A distância com a menor diferença para com a altura real é a utilizada durante as medições.

Para avaliar o sistema diversas medições foram realizadas de diversos objetos. O principal objeto de avaliação são duas esferas com distância entre seus centros calibrada. A bancada foi utilizada para comparar os resultados do ajuste polinomial e dos algoritmos desenvolvidos tanto no ar quanto na água. Foram avaliados também a consideração de apenas uma refração ou duas refrações na janela dos sistema e a utilização de uma ou mais aquisições do degrau para otimização da distância da janela. A consideração de uma refração provou-se superior à de duas refrações e ao menos três imagens do degrau fora necessárias

para calibrar o sistema na melhor distância de janela. Os resultado do método proposto e do ajuste polinomial foram bastante semelhantes tanto no ar quanto na água, sendo as medições na água com menores erros do que as medições no ar, consequência da diminuição do cone de visão no ambiente subaquático, resultando em uma melhor resolução.

Assim, o sistema desenvolvido, composto tanto dos componentes físicos quanto dos algoritmos provou-se capaz de realizar as medições em laboratório, tendo resultados próximos ao método de referência. Possíveis trabalhos futuros incluem o acoplamento do sensor a módulos de movimentação, como ROVs, para a realização de medições fora do laboratório.

Palavras-chave: Digitalização subaquática. Sensores de triangulação laser. Modelo de refração. Projeto óptico.

ABSTRACT

Underwater tridimensional measurement has many applications, for example, to control underwater equipment during optimized maintenance procedures in the oil and gas industry. Systems with laser triangulation sensors (LTS) are being used underwater at present and some underwater problems with LTS have already been discussed. Among these challenging obstacles are poor image quality, due to light absorption and backscattering, and refraction, due to optical window interfaces between water and air inside the camera chamber. The refraction effect can be predicted knowing the distance from the camera pinhole center to the surface of refraction, the axis of refraction, the refractive index of the mediums and the thickness of the optical window. This work analyses two methods for underwater LTS calibration using real experiments with a built LTS, in-air and underwater. The first method uses a polynomial adjustment correlating to the laser peak for each camera image line with a 3D point. This method needs a complete calibration in the underwater environment. The second method proposed is based on the pinhole camera model and a fitted mathematical plane for the projected laser light plane. In air measurements, a line can be defined through the lens center using the pinhole projection matrix for each laser peak detected in the image. The intersection of this line with the laser mathematical plane leads to a measured 3D point. For high quality underwater LTS measurements, it is necessary to additionally consider the refraction effect on the window and water interface. Considering the optical window normal to the camera axis, a ray path is defined on the plane of refraction according to the Snell's law to intercept the laser plane, defining a 3D point. The calibration for underwater measurement needs to estimate the window distance from the camera. In the proposed method, after the in-air calibration, a step standard is measured underwater and the window distance from the camera is optimized. The method is evaluated according to the guidelines of VDI/VDE 2634 and multiple objects were evaluated.

Keywords: Underwater digitalization. Laser triangulation sensors. Refraction modelling. Optical design.

LIST OF FIGURES

Figure 1 Images from different sonar types. (HORNER et al., 2009; COIRAS; PETILLOT; LANE, 2007) 31
Figure 2 Acoustic lens schematic. (ROSENBLUM; KAMGAR-PARSI, 1992) 31
Figure 3 Echoscope equipment and measurement result. (CODAOCTOPUS..., 2017; CRISP..., 2017) 32
Figure 4 BlueView equipment and measurement result.(BLUVIEW..., 2017; BLUEVIEW..., 2017) 32
Figure 5 Scopos Investigator equipment, measurement result and subject. (SCOPOS..., 2017; SUBSEA..., 2017) 33
Figure 6 STIL technique. (MCLEAN, 1999) 34
Figure 7 Pinhole camera schematic. (PINHOLE..., 2017) 34
Figure 8 Pinhole mathematical model. Adapted from Hartley and Zisserman (2004) 35
Figure 9 Stereo system. (CHOOSING..., 2017) 39
Figure 10 Homologous points and epipolar geometry in stereo vision. Source: Author's own work 40
Figure 11 Commercial active stereo systems. Source: Author's own work 40
Figure 12 Accuity laser. (COMPACT..., 2017) 41
Figure 13 2G Robotics underwater laser triangulation sensor and measurement example. (ULS-500..., 2017; OFFSHORE..., 2017) 42
Figure 14 Laser triangulation model. Adapted from Gan and Tang (2011) 43
Figure 15 Uncertainty limit for a LTS.(DORSCH; HÄUSLER; HERRMANN, 1994) 44
Figure 16 Scheimpflug configuration in a LTS. Adapted from Gan and Tang (2011) 45
Figure 17 The standoff of a LTS is in the middle of the measurement range. Source: Author's own work 46
Figure 18 Occlusion during measurement. Source: Author's own work 47
Figure 19 Laser plane fitting measurement. (SANTOLARIA et al., 2009) 48

Figure 20 Light absorption in different oceans. 1 is in the Central Pacific; a very clear, deep-sea water, 6 is in the Atlantic ocean, (WOZNIAK; DERA, 2007) 50
Figure 21 Image of the same pattern in the same position, with and without water, respectively. The images were captured through a flat glass and the optical axis was normal to the glass. Source: Author's own work 51
Figure 22 Refraction model. Adapted from Glassner (1989) 52
Figure 23 Dome window correcting the refraction. (NEWTON; BALDWIN; FRYER, 1989) 54
Figure 24 Non-SVP while looking through a flat interface. (TREIBITZ; SCHECHNER; SINGH, 2008) 55
Figure 25 Multi-layer flat refractive geometry. (AGRAWAL et al., 2012) 56
Figure 26 Designed sensor. Source: Author's own work 60
Figure 27 Inscribed pentagon side sized in a 300 mm diameter circle. Source: Author's own work 61
Figure 28 LTS 3D model optimization with in-air values. Source: Author's own work 62
Figure 29 Angled wall water tank used in final evaluation. Source: Author's own work 63
Figure 30 Camera positioning.(a) The positioning 'U' shape.(b) The camera fixed on the 'U' shapes. (c) The auxiliary fixing element positioning. (d) The camera mounted on the auxiliary element. (e) The auxiliary positioning element with respect to the lid. (f) The camera mounted on the lid. Source: Author's own work .. 64
Figure 31 Laser positioning. Source: Author's own work 65
Figure 32 Details of the back flanges. Source: Author's own work 66
Figure 33 Clamped and unclassified configurations.(HARRIS, 1999) 66
Figure 34 Window resistance values. (HARRIS, 1999) 67
Figure 35 Sensor fixing during calibration. Source: Author's own work 67
Figure 36 Back and superior fixing holes for auxiliary moving systems. Source: Author's own work 68
Figure 37 Hardware used to build the LTS. (MQ013MG-E2, 2017; HF12..., 2017; MINI..., 2017) 68
Figure 38 Built LTS. (a) is the camera module and (b) is the laser

module. Source: Author's own work 69
Figure 39 Complete measuring bench: displacement system (a), hydraulic system (b) and mounting structure (c). Source: Author's own work 70
Figure 40 The linear slide and the motor. Source: Author's own work 71
Figure 41 Mounting structure details. Source: Author's own work 72
Figure 42 Measurement model. Source: Author's own work 73
Figure 43 Measurement procedure. Source: Author's own work... 74
Figure 44 Resulting image from the step standard used during window distance calibration. Source: Author's own work 76
Figure 45 3D point result for different window distances d. Source: Author's own work 77
Figure 46 Calibration procedure. Source: Author's own work..... 77
Figure 47 Evaluation objects: two fixed spheres, welding beads, a plane and a dummy head. Source: Author's own work 80
Figure 48 Calibration Standard. Source: Author's own work 82
Figure 49 Step Standard. Source: Author's own work 82
Figure 50 Calibration layout used to adjust the laser and the camera, also showing the OCS. Source: Author's own work 83
Figure 51 Calibration layout used to acquire the calibration images. First the table is aligned (a), then the LTS is aligned (b), both with a spirit level. Source: Author's own work 84
Figure 52 Acquisition layout. Source: Author's own work 86
Figure 53 First, the original acquired image, then the processing result and the labels. Source: Author's own work 87
Figure 54 Laser image processing to peak search. First, the original image, then, the filter and the laser peak position (not shown with subpixel resolution). Source: Author's own work 87
Figure 55 Sphere acquisitions.(a-c) images shown in-air. (d-f) images underwater. Respectively close to the system, on the stand off and farther from the system. Source: Author's own work 88
Figure 56 (a) (c) and (e) are in-air images. (b) (d) and (f) are underwater images. Respectively from the dummy head, the welding beads and the PVC tube. Source: Author's own work 90
Figure 57 Sensor movement direction during acquisitions. Source: Author's own work 91
Figure 58 Z(v) polynomials examples from one of the top, middle

and bottom image lines, in-air and underwater. Source: Author's own work 92
Figure 59 Y(Z) polynomials examples from one of the top, middle and bottom image lines, in-air and underwater. Source: Author's own work 93
Figure 60 Dummy head measurements in-air and underwater using the polynomial adjustment. Source: Author's own work 94
Figure 61 Welding bead measurements in-air and underwater using the polynomial adjustment. Source: Author's own work 95
Figure 62 300 mm diameter pipe measurements in-air and underwater with the polynomial method. Source: Author's own work .. 95
Figure 63 Dummy head measurements in-air (a) and underwater (b) with the proposed method. Source: Author's own work 100
Figure 64 Welding bead measurements in-air and underwater using the proposed method. Source: Author's own work 100
Figure 65 300 mm diameter pipe measurements in-air (a) and underwater (b) with the proposed method. Source: Author's own work 101
Figure 66 Comparison of all the measurement results. Source: Author's own work 102
Figure 67 Y direction measurement volume. Source: Author's own work 105

LIST OF TABLES

Table 1 System parameters 63
Table 2 Underwater sphere measurement errors for the polynomial adjustment. The worst measurement for each parameter is highlighted 93
Table 3 in-air and underwater plane measurement errors for the polynomial adjustment. 94
Table 4 Relation between the number of step standard images used during calibration and the refractive window distance 97
Table 5 Measurement errors considering one or two refractions during spheres evaluation. 98
Table 6 Underwater sphere measurement errors for the proposed method. The worst measurement for each parameter is highlighted 99
Table 7 Underwater plane measurement errors for the proposed method. 99
Table 8 Spheres spacing percent error 103
Table 9 Proposed method underwater uncertainty evaluation 104

LIST OF ABBREVIATIONS

AUV	Autonomous Underwater Vehicle
CCS	Camera Coordinate System
CMM	Coordinate Measuring Machine
DLT	Direct Linear Transformation
FOV	Field of View
LTS	Laser Triangulation System
OCS	Object Coordinate System
PC	Personal Computer
PE	Probing Error
PVC	Polyvinyl chloride
ROV	Remotely Operated System
SLAM	Simultaneous Localization and mapping
Sonar	Sound Navigation and Ranging
SSE	Sphere Spacing Error
SVP	Single View Point
ToF	Time of Flight
USB	Universal Serial Bus

LIST OF SYMBOLS

$\underline{\mathrm{X}}$	3D coordinate in OCS
$\underline{\mathrm{x}}$	Image coordinate
$\underline{\mathrm{C}}$	Camera pinhole center
$\underline{\mathrm{P}}$	Projection matrix
K	Intrinsic parameters matrix
R	Rotation matrix
t	Translation matrix
θ_t	Triangulation angle
f	Focal length
$\hat{x}, \hat{y}$	Undistorted image coordinates
k_1, k_2	Radial distortion coefficients
π	Image plane
B	Baseline
θ_t	Triangulation angle
s_x, s_y	Pixel size
λ	Light wavelength
β_s	Scheimpflug condition angle
k	Lens magnification factor
η	Medium index of refraction
v_n	Vector during refraction on layer n
d	Distance from the camera pinhole center point to the plane of refraction
$\mathbf{T}$	Transmitted ray
$\mathbf{I}$	Incidence ray
$\mathbf{N}$	Refraction interface normal vector
θ_T	Transmitted angle
θ_I	Incidence angle
t_w	Window thickness
A_w	Unsupported aperture diameter
δP_w	Pressure differential
S_f	Fracture strength
$\mathbf{N}$	Refraction interface normal vector

ν Degrees of freedom

CONTENTS

1 INTRODUCTION 25
1.1 WORK PURPOSES 26
1.2 WORK OVERVIEW 26
2 UNDERWATER MEASUREMENTS 29
2.1 MAIN METHODS 29
2.1.1 Sonars 29
2.1.2 LiDAR 31
2.1.3 Photogrammetry 33
2.1.4 Laser Triangulation Systems 41
2.1.4.1 Laser Triangulation Principle 41
2.1.4.2 Laser Plane Fitting Calibration 47
2.1.4.3 Polynomial Regression Calibration 49
2.2 INFLUENCES ON UNDERWATER IMAGES 50
2.3 UNDERWATER CAMERA CALIBRATION 55
3 UNDERWATER DEVELOPED SENSOR 59
3.1 MECHANICAL DESIGN 59
3.1.1 Design Requirements 59
3.1.2 System Design 60
3.1.3 Measuring Bench 70
3.2 DEVELOPED ALGORITHMS 72
3.2.1 Measurement Algorithm 72
3.2.2 Refraction Calibration Algorithm 76
4 SYSTEM EVALUATION 79
4.1 EVALUATION OBJECTS 79
4.2 CALIBRATION STANDARDS 81
4.3 CALIBRATION LAYOUT 83
4.4 ACQUISITION LAYOUT 85
4.5 IMAGES PROCESSING 86
4.6 ACQUIRED IMAGES 87
4.7 POLYNOMIAL CALIBRATION 92
4.7.1 Polynomial Adjustment Results 93
4.8 PROPOSED CALIBRATION 96
4.8.1 Number of Underwater Images to Calibrate d 96
4.8.2 Refraction between Glass and Air 97
4.8.3 Proposed Method Results 98
4.8.4 Results Comparison 102

4.8.5 Uncertainty Evaluation for the Proposed Method Underwater 103
4.8.6 Y Direction Measurement Length 105
5 CONCLUSIONS 107
5.1 FUTURE WORKS 108
References 109

1 INTRODUCTION

Underwater tridimensional measurement has many applications, in the oil and gas industry. The area of interest of the present work, for example, are the applications on the underwater equipment control and maintenance procedure optimization. Other applications include archeology (DRAP et al., 2007) and biology(GIBSON; ATKINSON; GORDON, 2016) investigation.

Multiple techniques can be used in these environments to acquire distances and geometrical information, such as Sound Navigation and Ranging (sonar) and Light Detection and Ranging (LiDAR). However, the optical techniques are, still, the most suitable ones for close range measuring, up to 10 m. Among the optical techniques, some that can be adapted for underwater measurements are stereo vision, simultaneous localization and mapping (SLAM), and laser triangulation sensors (LTS). All of these techniques have advantages and disadvantages, mainly that acoustic techniques, such as the sonar, have the best performance for long range measurements, greater than 10 m and the optical methods have the smallest uncertainties for close range measurements.

The LTS is a very known technique in air (BESL, 1988; JI; LEU, 1989a) and some underwater problems with the LTS have already been discussed in other works (CACCIA, 2006; CHANTLER; CLARK; UMASUTHAN, 1997), a few of these obstacles are light absorption, light scattering, and refraction.

Overcoming these obstacles is a fundamental step to obtain reliable 3D information with a LTS. Light absorption and scattering can be diminished, for example, by selecting the right wavelength and the refraction can be considered in the measurement procedure. These steps can take the underwater measurement uncertainties closer to the in-air uncertainties.

This work, then, proposed a LTS design and a method for its measuring and calibrating procedures. The LTS was built in order to achieve some objectives, such as measuring a 300 mm diameter pipe with an uncertainty of a tenth of a millimeter as well as maintaining a safe distance from the measured subject.

Along with the built sensor, a method for calibration and measuring was proposed and evaluated. This method is based on the estimation of the refractive window distance from the camera center. This distance is ray traced from the camera to the laser plane and creates

the point cloud. The method is compared with a reference calibration to evaluate its effectiveness.

1.1 WORK PURPOSES

The main objective of this work is to design, build and validate a light sheet laser triangulation system for underwater environment operation up to 5 m deep. This sensor must consider the additional effects due to the refraction and it must be able to acquire quality underwater images, resulting in a reliable three-dimensional point cloud.

The specifics objectives of this work are:

- Develop calibration and measurement algorithms specific to underwater measurements with laser triangulation systems, taking into account the refraction effect.

- Flexible, compact and modular mechanical design for underwater applications. The systems design must consider the attachment to measurement robots, linear guides, ROVs or underwater robots.

- Extract quantitative parameters from scenes and objects of interest, through three-dimensional measurements and be able to consider the system movement to allow point cloud concatenation.

- Evaluate the developed system errors.

1.2 WORK OVERVIEW

This work is divided into five main chapters: introduction, underwater measurements, underwater developed sensor, system evaluation and conclusion.

The introduction presents the motivation to build an underwater LTS, the objectives to achieve the desired sensor and the work overview.

Underwater measurements presents the main methods to achieve underwater digitalization and the challenges in underwater environments. The main methods covered are sonar, LiDAR and photogrammetry techniques. A more detailed description is given to the laser triangulation method and the main obstacles are focused in underwater images.

Underwater developed sensor presents the designed and built LTS and its algorithms. All the calculations and simulations to achieve the chosen sensor characteristics are described. Followed by the description of the algorithms applied to the calibration and measurement.

System evaluation presents the evaluation to estimate the sensor errors with the proposed method and a reference polynomial adjustment method, both underwater and in air. Multiple objects were measured to evaluate the capabilities of the sensor.

In the conclusion, the methods are compared and some observations are made along with proposed future works for the designed sensor.

2 UNDERWATER MEASUREMENTS

Three dimensional measurements of underwater environments are useful on many applications. The oil and gas industry utilizes a lot of equipment for oil extraction that need constant maintenance (DEY; OGUNLANA; NAKSUKSAKUL, 2004), biologist have great interest in investigating the underwater life abundance (GIBSON; ATKINSON; GORDON, 2016) and archaeological sites provide historical knowledge (DRAP et al., 2007). Usually light and sound are used as means to gather the measurement information. However, it is not always an easy task to obtain reliable underwater point clouds, because the light scatters, is absorbed and refracts and the sound cannot always provide a good resolution. These obstacles must be considered to reach optimal measurement results.

There are a few methods used nowadays in a varying number of applications. A brief review of the main methods will be made showing their results, advantages and disadvantages. After this review, the laser triangulation method, the focus of this work, will be explained more deeply.

2.1 MAIN METHODS

Underwater 3D reconstruction methods can be divided in time of flight (ToF) techniques and triangulation techniques (MASSOT-CAMPOS; OLIVER-CODINA, 2015). The ToF methods are, for example, sonar and LiDAR and some of the triangulation methods are stereo vision and laser triangulation.

2.1.1 Sonars

Sonar is a widely used ToF technique in maritime vessels to obtain depths and sea floor information. They are also used in SLAM applications, associated with remotely operated vehicles(ROVs) (RIBAS et al., 2006). Nonetheless, they can also be used in three-dimensional measurements being, sometimes, called acoustic chambers or acoustic cameras (TAO et al., 2003; ROSENBLUM; KAMGAR-PARSI, 1992).

Sonar systems create a pulse of sound and wait for its reflection. The time of reflection is then correlated with the object distance. Since

sound propagates well underwater, they can reach distances as far as kilometers and can operate with little to zero visibility conditions. However, they also have higher uncertainties in close range measurements, when compared with other digitalization method, such as optical ones (MASSOT-CAMPOS; OLIVER-CODINA, 2015).

Because the measurement is dependent on the sound wave propagation speed, this is a source of uncertainties. The propagation speed underwater is determined by the medium pressure, which changes with depth and density, which changes with temperature and salinity. (DIVISION; DIVISION; ECKART, 1946)

The simplest sonar is the single forward looking beam. After the signal generation, the beam is shaped within the desired angle and direction. Then, the resulting image has information of azimuth and distance, but the elevation cannot be acquired with a single acquisition.

However, aside from using a single beam (GUO, 2013; HORNER et al., 2009) a sonar can also use multiple beams (PATHAK; BIRK; VASKEVICIUS, 2010) or side beams (COIRAS; PETILLOT; LANE, 2007; ROSENBLUM; KAMGAR-PARSI, 1992) to gather data. To create a point cloud, the single beam must be moved with a known distance and orientation, but the multiple beams can create a 3D reconstruction with a single acquisition. The side beam sonar uses a beam in the form of cone that can later be processed to acquire a three dimensional point cloud (COIRAS; PETILLOT; LANE, 2007).

The acquisition result of a single beam sonar is shown in Figure 1 a. The elevation is lost during acquisition, the distance is the Y axis and the azimuth is the angle. A side scan sonar image is shown in Figure 1 b. The image is equivalent to a photo, because the lost information is the depth.

Sonar with low frequency can survey wide areas of the ocean floor, but can only distinguish features larger than tens of meters. On the other hand, the resolution is proportional to the frequency and side scan sonar can produce dozens of millimeters of resolution, in exchange for a loss in range.

The acoustic lens are a set of highly directional acoustic transducers attached to a shell forming a retina, shown in Figure 2. . This way, the delay has the range information and the transducer position estimation that provides the azimuth and elevation, allowing a full 3D reconstruction.

One example of a commercial 3D sonar is the Echoscope in Figure 3, an acoustic chamber ultrasound 3D inspection system with a resolution of 30 mm and a maximum reach of 120 m.

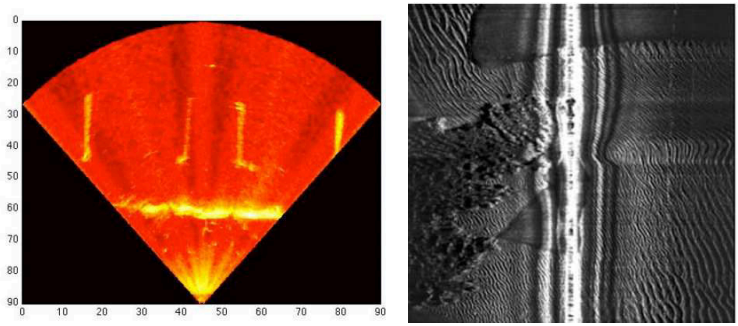

(a) Single beam sonar image (b) Side scan sonar image

Figure 1: Images from different sonar types. (HORNER et al., 2009; COIRAS; PETILLOT; LANE, 2007)

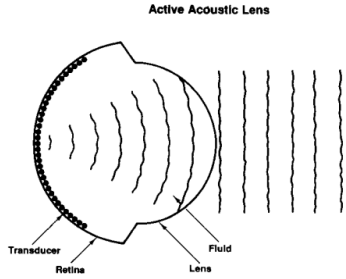

Figure 2: Acoustic lens schematic. (ROSENBLUM; KAMGAR-PARSI, 1992)

Another example of sonar is the BV5000 in Figure 4 manufactured by BlueView. It also makes 3D measurements and enables integration with laser triangulation systems. It has a resolution of 10 mm and a maximum reach of 10 m.

2.1.2 LiDAR

Light detecting and ranging (LiDAR) is a ToF technique, such as the sonar, but it uses light signals. Some in-air systems can reach resolutions of 0.8 mm in a 10 m range (SCAN..., 2017).). Consider-

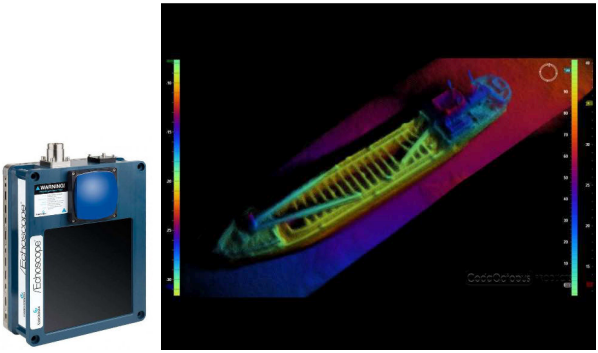

Figure 3: Echoscope equipment and measurement result. (CODAOCTOPUS..., 2017; CRISP..., 2017)

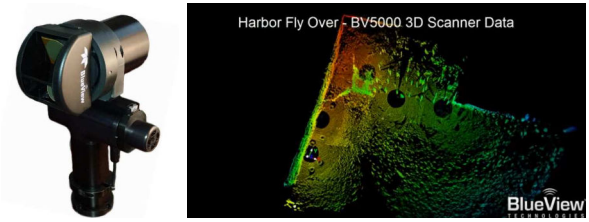

Figure 4: BlueView equipment and measurement result.(BLUVIEW..., 2017; BLUEVIEW..., 2017)

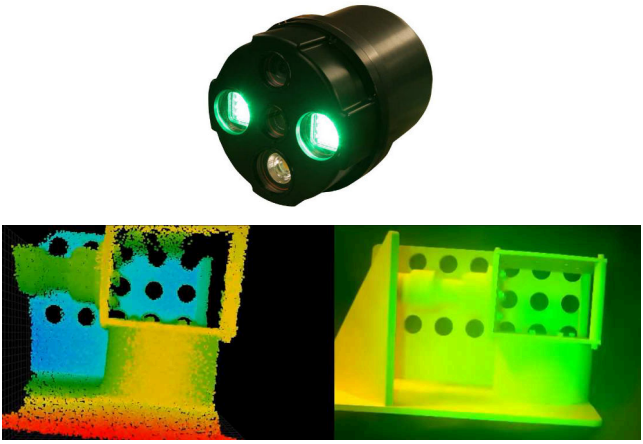

Figure 5: Scopos Investigator equipment, measurement result and subject. (SCOPOS..., 2017; SUBSEA..., 2017)

ing underwater applications, most LiDAR systems are used as airborne scanners being able to recover both the surface and the sea bottom resulting in a high range reconstruction (MASSOT-CAMPOS; OLIVER-CODINA, 2015). LiDAR systems are also used in underwater ranging applications, where only the distance is obtained (WALDRON; MULLEN, 2009). However, one commercial system built for underwater measurements is the Scopos Investigaton 5, which has two ranges: 250 m and 1500 m and the resolutions are not given by the manufacturer.

Another LiDAR technique is the Streak Tube Imaging LiDAR (STIL), which is very similar to the single-beam sonar technique (MCLEAN, 1999). A cylindrical lens is used to form a fan beam and a photocathode with a slit and a sweep plate is used to resolve the range and azimuth data. The process is repeated as the aircraft moves forward and a full 3D image is obtained as shown in Figure 6. The sensor can reach a 10 m range with 2.6 mm resolution.

2.1.3 Photogrammetry

In the photogrammetry techniques, images are used to create a 3D point cloud. A camera or set of cameras and passive or active techniques are used to obtain the three-dimensional points. While

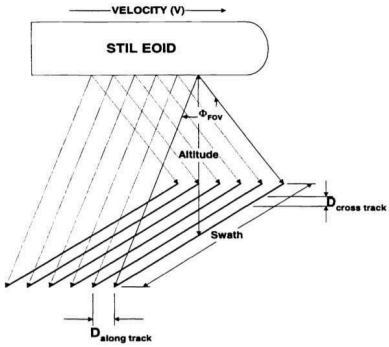

Figure 6: STIL technique. (MCLEAN, 1999)

underwater, the light is highly attenuated, meaning that the range of measurement for these kinds of sensors is much smaller than the sonar. However, much smaller uncertainties can be achieved using these techniques (MASSOT-CAMPOS; OLIVER-CODINA, 2015). Stereo vision, structure from motion and laser triangulation are some of the most commonly used photogrammetry techniques. Since the main focus of this work is the laser triangulation technique, it will be presented in a separate section.

Camera calibration is an important component for various photogrammetry techniques. The main camera calibration method considers a pinhole model, in which all rays pass through a small hole in a closed box. These rays form, on the opposite side of the box an upside down image, as shown in Figure 7. (HARTLEY; ZISSERMAN, 2004)

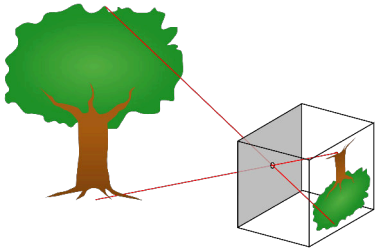

Figure 7: Pinhole camera schematic. (PINHOLE..., 2017)

To simplify this model the image plane is considered between the

pinhole center and the object. So, considering Figure 8, a point **X** in 3D object coordinate system (OCS) being observed by a camera with a projection center or pupil **C** and an image plane. The **X** projection on the image plane will be **x**, which is the result of the crossing between the line from **X** through the pinhole center **C** and the image plane.

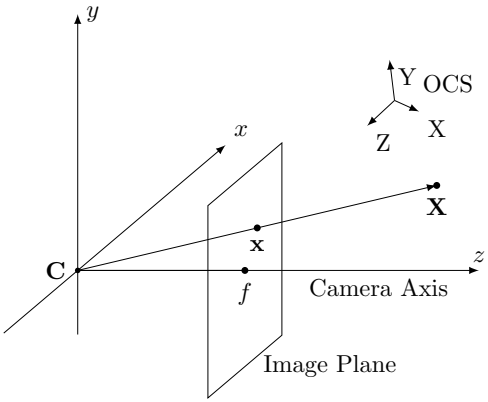

Figure 8: Pinhole mathematical model. Adapted from Hartley and Zisserman (2004).

In this model, the calibration parameter is the projection matrix, the matrix that projects the 3D point **X** in OCS to its respective projected camera pixel **x**. The projection matrix **P** is a 3x4 matrix that contains both the extrinsic and intrinsic parameters of the camera. The extrinsic parameters are the rotation and translation matrices $[R \quad t]$ that transform the 3D coordinates from the OCS to the CCS. The intrinsic parameters are the focal point f and the principal sensor point, coordinates x_0 and y_0, which allows the CCS shift to the center of the imaging sensor.(HARTLEY; ZISSERMAN, 2004)

$$\mathbf{x} = \mathbf{PX} \tag{2.1}$$

Where $\mathbf{P} = K[R \quad t]$, K is a 3×3 matrix and $[R \quad t]$ is a 3×4 matrix that contains the rotation, R in a 3×3 matrix and the translation in a 3×1 matrix.

Matrix K contains the intrinsic parameters and is as follows:

$$K = \begin{bmatrix} f_x & 0 & x_0 \\ 0 & f_y & y_0 \\ 0 & 0 & 1 \end{bmatrix}$$

Where f_x and f_y are the camera'focal length and x_0 and y_0 are the camera's principal point in CCS.

There are many ways to obtain the camera projection matrix, two main methods will be presented. Both methods need a set of 3D points and its image correspondence. The problem with finding the projection matrix with these conditions is called the resection problem. The first approach is the direct linear transformation (DLT) method and the other uses plane homographies. After the applied method, some optimization techniques are applied, such as the Levenberg-Marquardt algorithm (LOURAKIS, 2005).

The DLT approach formulates a homogeneous, usually overdetermined, linear system of equations and solves this by finding an approximate null space. Let p_i, $i = 1, 2, 3$ be the 4×1 vectors containing the rows of projection matrix P, that is

$$P = \begin{bmatrix} p_1^T \\ p_2^T \\ p_3^T \end{bmatrix}$$

And $\mathbf{PX}$ can be written as

$$\mathbf{PX} = \begin{bmatrix} p_1^T \mathbf{X} \\ p_2^T \mathbf{X} \\ p_3^T \mathbf{X} \end{bmatrix}$$

Since $\mathbf{x} = \mathbf{PX}$ the cross product $\mathbf{x} \times \mathbf{PX}$ is zero. Considering $\mathbf{x} = (x, y, 1)$, since $\mathbf{x}$ is in homogeneous coordinates, this cross product can be written explicitly as

$$\mathbf{x} \times \mathbf{PX} = \begin{bmatrix} y\, p_3^T \mathbf{X} - p_2^T \mathbf{X} \\ p_1^T \mathbf{X} - x\, p_3^T \mathbf{X} \\ x\, p_2^T \mathbf{X} - y\, p_1^T \mathbf{X} \end{bmatrix}$$

Then, since $p_i^T \mathbf{X} = \mathbf{X}^T p_i$ and isolating the variable p_i

$$\begin{bmatrix} 0 & -\mathbf{X} & y\,\mathbf{X} \\ \mathbf{X} & 0 & -x\,\mathbf{X} \\ y\,\mathbf{X} & x\,\mathbf{X} & 0 \end{bmatrix} \begin{bmatrix} p_1 \\ p_2 \\ p_3 \end{bmatrix} = 0$$

Where each 0 represents a 1×4 null matrix, resulting in a linear system $Ax = 0$. In addition, because the third row can be written as a combination of the first two rows, matrix A is singular, thus the linear equations to be solved are

$$\begin{bmatrix} 0 & -\mathbf{X} & y\,\mathbf{X} \\ \mathbf{X} & 0 & -x\,\mathbf{X} \end{bmatrix} \begin{bmatrix} p_1 \\ p_2 \\ p_3 \end{bmatrix} = 0$$

Because the matrix can be scaled, there are 8 variables and since each point leads to two equations, a 4 point set leads to an exact solution. However, since the system is affected by image noise, more points leading to an overdetermined system is a more viable solution. One way to find the A matrix null space approximation is through the eigenvector with the smallest eigenvector of $A^T A$. But, this is a poorly conditioned matrix since the third column will be orders of magnitude higher than the other columns, considering that the image coordinates can be as large as thousands of pixels. This can be solved normalizing the data before matrix A is built. The image points can be normalized by translating every point so the centroid of the points is the system coordinate center and scaled so the average points distance to the center is $\sqrt{2}$ resulting in average point of (1,1). The 3D points can be normalized the same way but with an origin center distance of $\sqrt{3}$ so the average point is (1,1,1). This is a suitable normalization for most configurations. (HARTLEY; ZISSERMAN, 2004)

It follows that, the full projection matrix is obtained. Nevertheless, this method requires three dimensional standards, because the use of planar standard results in one coordinate always being null, which leads to a singular A matrix.

A second common way to calibrate a camera is through plane homographs (ZHANG, 1999). This method does not require a three dimensional standard, just a set of planar standard images with different rotations and translations is enough to provide the system calibration parameters. This method considers the Z coordinate to be null, thus,

$$s \begin{bmatrix} x \\ y \\ 1 \end{bmatrix} = K \begin{bmatrix} r_1 & r_2 & r_3 & t \end{bmatrix} \begin{bmatrix} X \\ Y \\ 0 \\ 1 \end{bmatrix} = K \begin{bmatrix} r_1 & r_2 & t \end{bmatrix} \begin{bmatrix} X \\ Y \\ 1 \end{bmatrix}$$

Being s a scalar factor. Considering a homography $\mathbf{H} = [h_1 h_2 h_3]$ is related to the projection matrix by

$$\begin{bmatrix} h_1 & h_2 & h_3 \end{bmatrix} = \phi K \begin{bmatrix} r_1 & r_2 & t \end{bmatrix}$$

Where ϕ is an arbitrary scalar. Since r_1 and r_2 are orthonormal

$$h_1^T K^{-T} K^{-1} h_2 = 0 \tag{2.2}$$

$$h_1^T K^{-T} K^{-1} h_1 = h_2^T K^{-T} K^{-1} h_2 \tag{2.3}$$

Considering $\mathbf{B} = \mathbf{A}^{-T}\mathbf{A}^{-}1$ and the vector $\mathbf{b} = [B_{11}, B_{12}, B_{22}, B_{23}, B_{33}]^T$ After some equations adjustments and considering

$$\mathbf{v}_{ij} = [h_{i1}h_{j1}, h_{i1}h_{j2}+h_{i2}h_{j1}, h_{i2}h_{j2}, h_{i3}h_{j1}+h_{i1}h_{j3}, h_{i3}h_{j2}+h_{i2}h_{j3}, h_{i3}h_{j3}]^T \tag{2.4}$$

The equation

$$\begin{bmatrix} \mathbf{v}_2^T \\ (\mathbf{v}_{11} - \mathbf{v}_{22})^T \end{bmatrix} \mathbf{b} = 0$$

Results in a likewise $Ax = 0$ equation system

$$\mathbf{V}\mathbf{b} = 0 \tag{2.5}$$

From the projection matrix, the intrinsic and extrinsic parameters can be separated. The translation is the fourth projection matrix column. The intrinsic parameters and the rotation are obtained from the three remaining columns. This is done by RQ-factorization, which separates one matrix into one right triangular and another as orthogonal, being the camera matrix as right triangular and the rotation as orthogonal. After this, the matrices must be scaled so that the third line, third element of the intrinsic parameters is one.

Besides the pinhole model, the lens distortions can also be estimated during calibration (BROWN, 1971). The lens distortions can be divided in radial and tangential distortions. In today's commercial lenses, the radial distortion is the most influential during image formation and usually just two coefficients are enough to correct the distorted image. (ZHANG, 1999). The optimization, then, has to find the optimal values for the equations

$$\hat{x} = x + x[k_1(x^2 + y^2) + k_2(x^2 + y^2)^2] \tag{2.6}$$

$$\hat{y} = y + y[k_1(x^2 + y^2) + k_2(x^2 + y^2)^2] \tag{2.7}$$

Where $\hat{x}$ and $\hat{y}$ and the normalized corrected pixel coordinates and k_1 and k_2 are the distortion coefficients.

After this estimation, the alternation between estimation of the

other parameters and the distortion coefficients are usually capable of evaluating the initial guesses to initialize the non-linear optimization. And finally, the calibration parameters are estimated to minimize the equations of both the projection matrix and the distortion coefficients.

The stereo vision techniques use two or more fixed cameras, as shown in Figure 9, to capture the scene and construct the point cloud. Through camera calibration, the position of one camera in respect to the others is solved and triangulation is possible using homologous points.

Figure 9: Stereo system. (CHOOSING..., 2017)

The homologous points are image points that represent the same 3D point in each different captured image of the scene, in Figure 10 the homologous points are $\mathbf{x}$ and $\mathbf{x'}$, respectively on the image planes π and π'. These image points are projected into lines from the image centers $\mathbf{C}$ and $\mathbf{C'}$ by applying the camera projection matrix. The cross between these lines is the measured 3D point $\mathbf{X}$. In practice, the lines do not cross due to image noise, so an approximation is made. The procedure is then repeated until a full point cloud is constructed.

In photogrammetry techniques, the homologous points used in triangulation can be obtained using passive or active techniques. The active methods use light with some kind of information projected onto the surface of interest while the passive illumination techniques do not project any additional information to the scene.

The fringe projection technique is an example of active photogrametry. The projected image has a sinusoidal pattern that assign a phase value for each image line or column. The use of calibrated cameras allows the epipolar geometry to be used. The epipolar geometry is built uniting the two pinhole centers generating the triangle shown in Figure 10. Then, the same phase is searched on the other images along the $\mathbf{l}$ line. The process is repeated for each image pixel and the

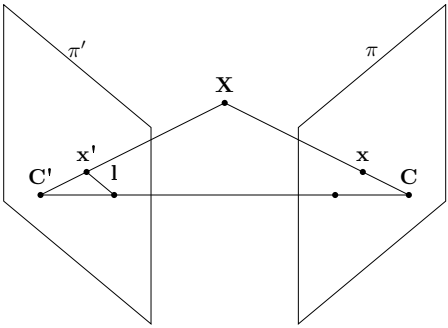

Figure 10: Homologous points and epipolar geometry in stereo vision. Source: Author's own work

point cloud is built. In Figure 11 a commercial system that uses fringe projection is presented. (HARTLEY; ZISSERMAN, 2004)

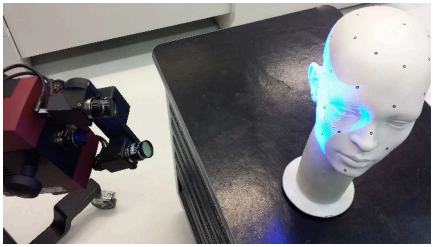

Figure 11: Commercial active stereo systems. Source: Author's own work

The passive illumination methods do not project any additional information on the surface of interest, for example the structure from motion technique (JORDT, 2014). In this technique, a single camera is moved whilst observing the surface of interest. After some image processing, the homologous points are established along with the camera position in each acquired image and the 3D mesh is constructed. These systems can easily be implemented in underwater environments, since all it needs is a moving camera that can be mounted, for example, on a ROV. All the image processing can be done after a video recording.

Stereo vision techniques are present in underwater measurements (BIANCO et al., 2013; BRUNO et al., 2011; BUSCHINELLI et al., 2016). The underwater environmental influences on images are further explored in the next sections.

2.1.4 Laser Triangulation Systems

A laser triangulation sensor (LTS) uses a laser projector and a camera to obtain required information, being, therefore, an active optical technique. Such information can be, for example, displacements, distances and three-dimensional points. The main principle behind LTS is the geometrical triangulation principle.

One example of commercial laser triangulation measurement sensor is the profiler scanCONTROL 2600-50 manufactured by Micro-Epsilon, presented in Figure 12, which presents a resolution of 4 µm and a measurement range of 60 mm.

Figure 12: Accuity laser. (COMPACT..., 2017)

Laser triangulation is one of the most used 3D underwater measurement methods. They have one of the lowest uncertainties among the presented methods and are used for short range measurements (up to 10 m), mainly due to light signal degradation.(MASSOT-CAMPOS; OLIVER-CODINA, 2015)

The company 2G Robotics has a LTS for underwater uses, shown in Figure 13, but the uncertainty is unspecified. The range goes from 0.13 m to 10 m and the resolution goes from 0.03 mm up to 0.31 mm, respectively.

2.1.4.1 Laser Triangulation Principle

The LTS uses some form of laser projection fixed with a certain distance and angle from a camera (JI; LEU, 1989b; GAN; TANG, 2011). The laser is, then, projected on a surface of interest and suffers some level of diffuse reflection. Some of the light rays from the surface pass through the focal point of the lens and the result of the intersection

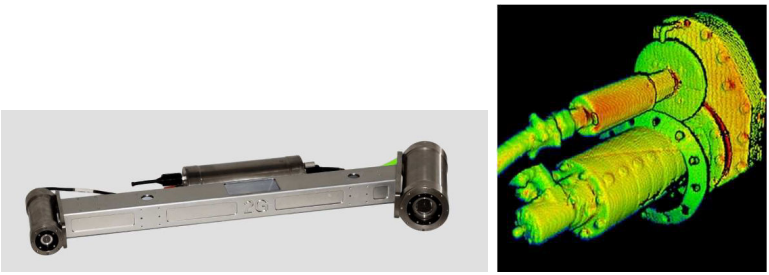

Figure 13: 2G Robotics underwater laser triangulation sensor and measurement example. (ULS-500..., 2017; OFFSHORE..., 2017)

between the laser and the surface is captured by an image sensor. In the captured image, the detected laser peak pixel can be associated with the desired dimension.

The simplest LTS is composed of a laser dot projector and a camera observing it with an angled view. As the camera observes an object getting closer to the laser, the laser image on the camera also moves along the image columns or lines. After proper calibration, the association between the distance from the laser and the image pixel position containing the laser peak can be done, resulting in distance measurement.

System characteristics such as, the measurement volume and the system resolution are defined by some parameters. The main system parameters, shown in Figure 14, are: the baseline B, the triangulation angle θ_t, the pinhole center point C given by the lens focal length f, the pixel size and the sensor resolution. One very important initial observation is that the relation between system resolution and measurement volume is inversely proportional considering the same sensor being used.

The baseline is the distance between the pinhole center and the laser projector. The triangulation angle is the angle between the camera axis and the laser optical axis. The pixel size and the resolution are characteristics of the sensor, and the pinhole center point depends on the selected lens. A relation between these characteristics and the system resolution can be derived, considering the sensor pixel size s_x and u the number of pixel from the image center and the CCS presented in 14. By triangle similarity (GAN; TANG, 2011)

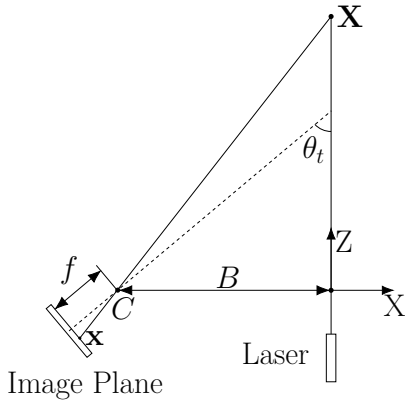

Figure 14: Laser triangulation model. Adapted from Gan and Tang (2011)

$$Z = \frac{Bf}{f \tan\theta_t - s_x u} \tag{2.8}$$

After the Eq. 2.8 derivative, the sensor resolution can be calculated, i.e. how the distance and pixel variation displacement are related. The derivative is (GAN; TANG, 2011)

$$\delta Z = \frac{Bf s_x}{(f \tan\theta_t - s_x u)^2} \delta u \tag{2.9}$$

This equation can be applied to estimate the sensor resolution along the Z coordinate. Since s_x is very small compared to f the factor inverse of $(f \tan\theta_t)^2$ is the most influential. The same procedure can be made in the Y direction, along the laser line in the captured image. Using the same similarity principle, Y is

$$Y = \frac{B \cos\theta_t f s_y v}{f \tan\theta_t - s_x u} \tag{2.10}$$

Which has a derivative

$$\delta Y = \frac{vB \cos\theta_t s_y s_x}{(f \tan\theta_t - s_x B \cos\theta_t)^2} \delta u + \frac{s_y B \cos\theta_t}{f \tan\theta_t - s_x u} \delta v \tag{2.11}$$

The defined object coordinate system is arbitrary and in this

case the X coordinate is always null.

The laser peak detection has a great influence on the measurement uncertainty. There are a few approaches to reach a sub pixel detection level. The center of mass, the zero crossing and the curve adjustment are some examples. There are some comparisons between methods with some advantage for the zero crossing method (NAIDU; FISHER, 1991).

The theoretical uncertainty limit is defined by the laser speckle (DORSCH; HÄUSLER; HERRMANN, 1994). The speckle occurs when coherent light is projected onto a diffuse surface. The coherence enables the constructive and destructive interference between the various laser reflections on the surface and a granular pattern is formed. The smaller the size of the speckle grain, the smaller the uncertainty limit, because the peak detection can be more exact. The speckle grain size characteristics depends on the wave length, the lens aperture and the distance between the camera and the measured surface. One way to make the grain smaller is to open the camera aperture. However, this also makes the depth of focus smaller, which makes the laser peak detection more inaccurate. Therefore, there is a compromised relation between the speckle grain size and the depth of focus length. In Figure 15 the relation between the detectable peak difference δx_{cog}, the light wavelength λ and the system angle of aperture u is shown.

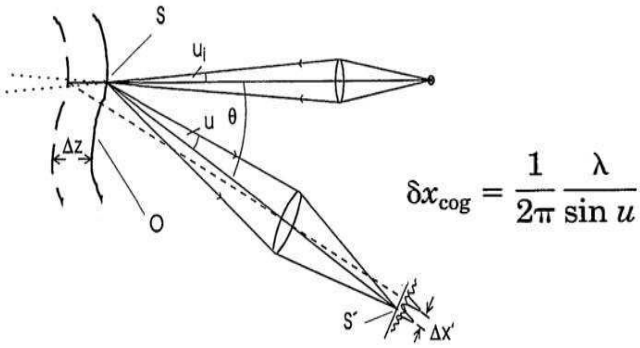

Figure 15: Uncertainty limit for a LTS.(DORSCH; HÄUSLER; HERRMANN, 1994)

The depth of focus influence can be minimized by applying the Scheimpflug principle which is widely used in LTS, with some consider-

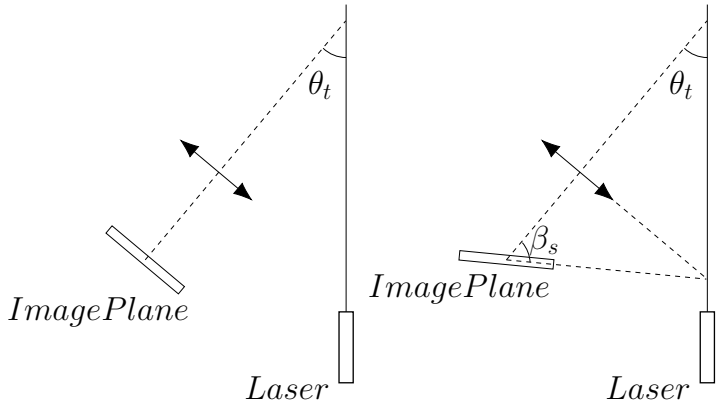

Figure 16: Scheimpflug configuration in a LTS. Adapted from Gan and Tang (2011)

ations (MIKS; NOVAK; NOVAK, 2013). The Scheimpflug condition is met when the angle between the image plane and the lens axis, as shown in Figure 16, β_s is

$$\tan\theta_t = k\tan\beta_s \tag{2.12}$$

Where k is the magnification factor. This is also called tilt and shift in photography. When the angle β_s, changes, the plane of focus also changes. Then, it is possible to always maintain the laser plane in focus, therefore, optimizing the measurements for all the measurement volume, since the portion of the image with the laser line will always be in focus. The sensor tilt enables a wider lens aperture, decreasing the speckle influence on the measurement.

Instead of projecting a dot, a line or multiple lines can be projected on the surface of interest. The line can capture more 3D points from the scene within a single image acquisition, since each laser peak for each image line or column is a 3D point. The multiple line projection has the advantage of measuring the sensor orientation with respect to the object with only one acquisition, since a plane can be adjusted with the captured information, but it requires multiple lasers or special optics.

A fundamental procedure to create a dense point cloud with a LTS is to move the sensor, because in one acquisition, only a small part of the object of interest is measured, only where the laser is hitting the

object. Therefore, the sensor must be mounted on equipment with known displacement, which can be a moving table, a robot or, in underwater cases, a ROV or autonomous underwater vehicle (AUV). This mounting requires another calibration to locate the sensor coordinate system in respect to the moving equipment coordinate system. One example of this calibration is to use an auxiliary object as a reference coordinate system (SANTOLARIA et al., 2009). This object has its coordinate system defined both by the LTS and an auxiliary machine, such as a coordinate measuring machine (CMM) Hence, the transformation between the LTS and the coupling between the sensor and the moving equipment coordinate system coordinate systems are possible.

Another important system characteristic is the stand-off, the optimal distance from the system to perform the measurement. It is the distance between the camera and the center of the measurement volume, as shown in Figure 17. The system parameters, such as lens and laser focus are adjusted for this distance. Accordingly, this is the best area in the measurement volume to acquire images.

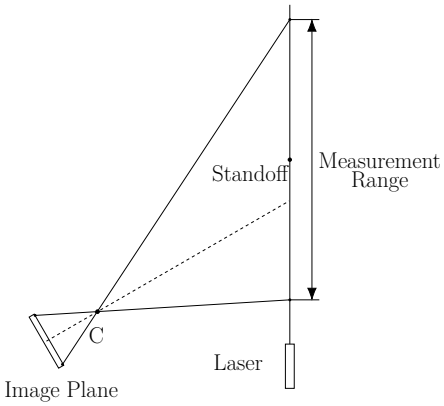

Figure 17: The standoff of a LTS is in the middle of the measurement range. Source: Author's own work

Some limitations in regards to the surface being measured and surface discontinuities appear during measurements with a LTS. Since the laser must be observed by the camera from an angled view, the surface must have some level of diffuse reflection, so the laser can be seen in the image. When the surface has low diffuse reflection, the laser power can be raised to get more light into the sensor. Surface discontinuities may cause occlusions during measurement, this occurs

when the own surface appears as an obstacle between the camera and the laser, as shown in Figure18. Therefore, when occlusions occur, the laser peak cannot be detected. Occlusions can be avoided by measuring the surface in different orientations.

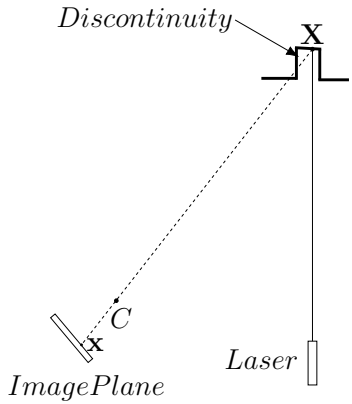

Figure 18: Occlusion during measurement. Source: Author's own work

The calibration of laser sheet sensors allows the acquired image to be transformed into three-dimensional points. Two calibration methods will be used in this work, both considering one laser line being projected. The first method considers a pinhole camera model and a mathematical plane (SANTOLARIA et al., 2009, 2011), in which it is necessary to calibrate both the camera and the laser plane. This method will be adapted to consider a refraction during measurement. The second method is a model-less method, with polynomials fitted for each line, relating the laser peak and the 3D point, this method will be used as a reference method.

2.1.4.2 Laser Plane Fitting Calibration

This calibration needs a calibrated camera, i.e. the intrinsic and extrinsic parameters must be estimated in a previous step. After the camera calibration, the laser plane fitting calibration is performed. It is based on approximating the laser plane as a mathematical plane with the plane coefficients according to the plane equation: $Ax + By + Cz + D = 0$. The measurement is based on projecting the detected laser peak, by applying the camera calibration parameters, and crossing this

projection with the mathematical plane, as shown in Figure 19.

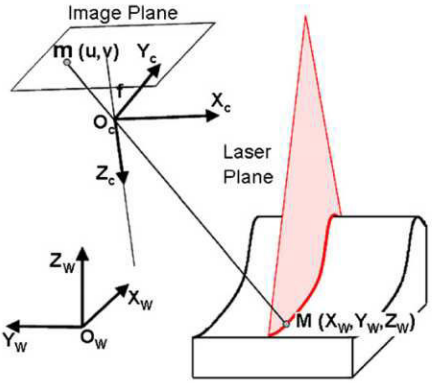

Figure 19: Laser plane fitting measurement. (SANTOLARIA et al., 2009)

To obtain the laser plane coefficients, a set of 3D points on the laser plane in various locations in the measurement volume is used to adjust a best fitted plane.

The plane point cloud can be obtained with a simple procedure, considering the OCS with X direction normal to the laser plane,the Z direction parallel to the laser projector axis and the origin at the measurement volume center. First, a plane with a known Z OCS coordinate on the XY plane containing the laser line is captured by the camera. After the image distortion correction, for each image line, the laser peak is detected and for each detected peak, a line is back projected to the OCS using the projection matrix. The projection provides two equations for a three variable system, which can be solved by the known Z coordinate. The process is then repeated for several Z coordinates until a laser plane point cloud is built and the mathematical plane is adjusted. The process can be improved by using the same image to calibrate the laser and the camera. Thus, ensuring that the plane images used are contained on the XY plane in OCS, since the OCS is defined during the camera calibration. Therefore, the plane movement during plane calibration is only in the Z direction.

Some sources of uncertainties arise during this kind of calibration. The moved plane flatness influences the measured points to construct the laser plane, because all the laser peaks are considered to be on the same Z coordinate. The plane displacement uncertainty leads to a different Z coordinate used in calibration. Also, since the laser plane

calibration and the measurement procedure use the projection matrix, the camera calibration errors have a direct influence on uncertainty measurement. Finally, the measurement quality is influenced by the laser light sheet quality, i.e. how 'flat'is the projected laser plane, this error can be minimized changing the adjusted surface to an equation that better represents the projected surface.

2.1.4.3 Polynomial Regression Calibration

This method correlates the laser peak and the 3D point through polynomial equations and is based on Trucco, Fisher and Fitzgibbon (1994). This is a 'black-box' approach, therefore the errors from camera and laser calibration, presented in the previous calibration, are absorbed into the adjusted equations. In this calibration, the ZY plane in OCS is considered to be on the laser plane, so the Y coordinate is aligned with the observed laser line and the X coordinate is always null. It is considered that the laser line captured on the image is along the image columns, therefore the peaks are established for each line.

A set of known 3D points and the images column with the laser peak are the variables and two polynomial equations are fitted for each image line.

The first polynomial equation correlates the image column pixel to the laser peak to the Z coordinate $P_u(v) = Z$ and the second polynomial equation correlates the Z coordinate to the Y coordinate $P_u(Z) = Y$. Polynomial equations must be adjusted since the sensitivity changes throughout the measurement volume, so the non-linearity is compensated. During the measurement, after the laser peak column is obtained, the Z coordinate is calculated with the first equation, then the Z is applied to the second equation. After that, the process is repeated for each image line.

The second equation is needed because of the camera amplification factor. Since the number of image lines is always the same, the Y variation for each line is bigger when the object is farther from the laser, so the Z distance for each line influences the Y coordinate.

The utilised 3D points to adjust the equations are the main source of uncertainties in this kind of calibration. If a moving plane is used to obtain the 3D points the plane flatness affects the considered 3D point errors, thus affecting the measurement uncertainty.

2.2 INFLUENCES ON UNDERWATER IMAGES

Underwater images taken with a camera inside housing are different than in air images, as the objects appear to be closer than they are and the observable distance is much lower. Light absorption, light scattering and refraction are the three main image quality and distortion influences when taking underwater images. They are dependent on many factors, some of which are, water salt concentration, particles in suspension and travelling light wavelength, thus all these factors have some kind of influence on the measurement result.

Light absorption occurs when the photons are absorbed while interacting with different particles in suspension in the water (WOZNIAK; DERA, 2007). Increasing the light source power can help reach a longer distance when this has a large influence. As shown in Figure 20, the light wave-length with the least underwater absorption is around 450 nm to 550 nm, the green and blue range. This is the reason why the ocean color is blue, because the most absorbed range is on the red spectrum.

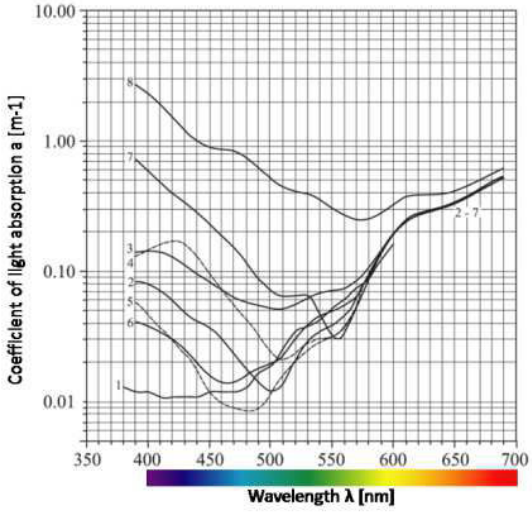

Figure 20: Light absorption in different oceans. 1 is in the Central Pacific; a very clear, deep-sea water, 6 is in the Atlantic ocean, (WOZNIAK; DERA, 2007)

Light scatter is divided in backscatter and forward scatter (SCHECHNER; KARPEL, 2005). They both occur when the light is deflected when colliding with particles in water. The deflection can occur guiding the light back to the receptor, backscattering, or to the object of interest, forward scattering. They have a higher influence on light propagation the more turbid the water is. When the light is backscattering, the increase in light power can decrease the image quality, since more light can come from scattering on the water itself than from the object of interest. The backscatter leads to a loss of contrast and the forward scatter causes a loss of sharpness. The use of higher wave-lengths reduces the scattering effect.

The light absorption and scattering are, then, on opposite sides. The least absorbed wave length is on the green and blue spectrum, but the least scattered is in the red spectrum. Generally, the green is chosen as a middle ground between the two, although for small ranges, the absorption does not play a major role, so the red spectrum is also usable.

Refraction is the light ray deflection when the transmission medium index of refraction changes. In underwater images, the refraction occurs on the interfaces between water, glass and air. The effect of a refraction in underwater images can be seen in Fig 21. The same pattern on the same distance and position from the camera is shown in both images, but the first one is underwater and the second in air. The refraction depends on the index of refraction of the medium, in the case of water, its index is dependent mainly on pressure, temperature, wavelength and salt concentration (QUAN; FRY, 1995).

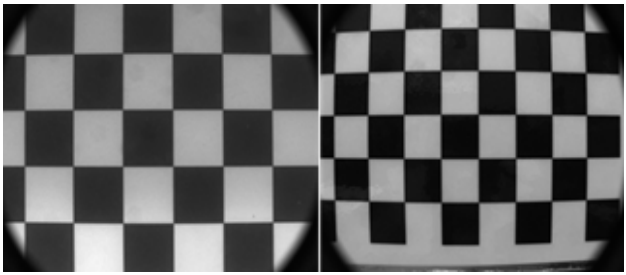

Figure 21: Image of the same pattern in the same position, with and without water, respectively. The images were captured through a flat glass and the optical axis was normal to the glass. Source: Author's own work

The refraction can be modelled (GLASSNER, 1989) as shown in Figure 22. The incidence ray **I** on a medium with index of refraction η_1 reaches a surface with an angle of incidence θ_i with respect to the vector **N**, which is normal to the interface of refraction. The ray is transmitted to the medium with index of refraction η_2 in the direction **T** with an angle of θ_t.

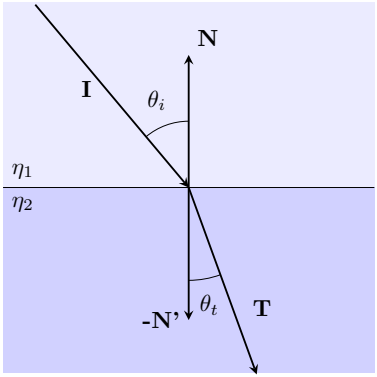

Figure 22: Refraction model. Adapted from Glassner (1989)

Because the transmitted ray is in the same plane as the normal and the incidence ray it can be written as a combination of both

$$\mathbf{T} = \alpha\mathbf{I} + \beta\mathbf{N} \tag{2.13}$$

The Snell' s Law states

$$\frac{\sin\theta_t}{\sin\theta_i} = \frac{\eta_i}{\eta_t} = \eta_{it} \tag{2.14}$$

From squaring both sides of Eq. 2.14

$$\sin^2\theta_i\,\eta_{it}^2 = \sin^2\theta_t \tag{2.15}$$

And because $\sin^2\theta + \cos^2\theta = 1$ and $(\mathbf{N}\cdot\mathbf{N}) = 1$

$$
\begin{aligned}
(1-\cos^2\theta_i)-1 &= \cos^2\theta_t \\
&= [-\mathbf{N}\cdot\mathbf{T}]^2 \\
&= [-\mathbf{N}\cdot(\alpha\mathbf{I}+\beta\mathbf{T})]^2 \\
&= [\alpha(-\mathbf{N}\cdot\mathbf{I})+\beta(-\mathbf{N}\cdot\mathbf{N})]^2 \\
&= [\alpha\cos\theta_1-\beta]^2
\end{aligned}
\tag{2.16}
$$

Because $\mathbf{T}$ has unit length

$$
\begin{aligned}
1 &= \mathbf{T}\cdot\mathbf{T} \\
&= (\alpha\mathbf{I}+\beta\mathbf{N})\cdot(\alpha\mathbf{I}+\beta\mathbf{N}) \\
&= \alpha^2(\mathbf{I}\cdot\mathbf{I})+2\alpha\beta(\mathbf{I}\cdot\mathbf{N})+\beta^2(\mathbf{N}\cdot\mathbf{N}) \\
&= \alpha^2-2\alpha\beta\cos\theta_i+\beta^2
\end{aligned}
\tag{2.17}
$$

By solving Eq.2.16 and Eq.2.17 for α and β and selecting the vector on the forth quadrant, the transmitted ray equation is

$$
\mathbf{T}=\eta_{it}\mathbf{I}+(\eta_{it}(\mathbf{N}\cdot\ -\mathbf{I})-\sqrt{(1+\eta_{it}^2((\mathbf{N}\cdot\ -\mathbf{I})^2-1))}\mathbf{N} \tag{2.18}
$$

Slight variations in the refractive index can cause a substantial difference in the acquired image, since an angle variation can represent many pixels in image coordinates. The refraction causes a problem described as a 3D distortion on the image (TREIBITZ; SCHECHNER; SINGH, 2008). It happens because the apparent focal length varies depending on the light ray incidence angle, thus the pinhole model, in which all the rays pass through a single point, which is not a physically valid model. One way around the refraction is the dome windows (NEWTON; BALDWIN; FRYER, 1989), as seen in Figure 23, they minimize the refraction effect acting as a slightly positive lens. They must be mounted so that the dome center of curvature is coincident with the pinhole center, which makes the dome specific for the designed lens and casing set.

All these factors have many impacts on both the designing underwater sensors and on the measurement method. The light source choice and considering the refraction during the measurement are some of the actions to minimize the various water effects. In the LTS case, i.e. short ranges, refraction is one of the most impacting effects, therefore,

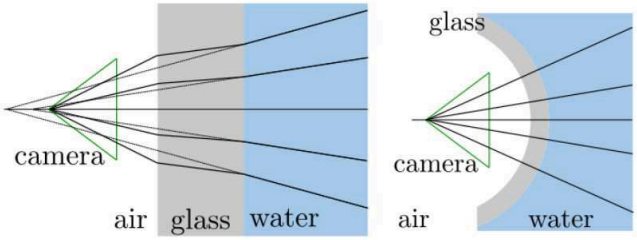

Figure 23: Dome window correcting the refraction. (NEWTON; BALDWIN; FRYER, 1989)

a calibration that takes this matter into account is essential.

2.3 UNDERWATER CAMERA CALIBRATION

The main effect to be considered during underwater camera calibration is refraction. The ray deflection caused by it can reflect into a several pixels position error. Refraction depends on the kind of housing being applied, domes and flat windows are the most commonly used. The flat window is the easiest to build, but the most influenced by the refraction. In this work, the main focus is to use the flat window and to predict the refraction using the measurement software, thus reducing the building costs. The camera in underwater environments inside a flat window housing is affected by a focal length variation effect, as shown in Figure 24, the objects appears to be bigger than when they are in-air, because of the reduced field of view (FOV). There are two main ways to counteract this effect: to consider the camera axial or to approximate this effect to a radial distortion also leading to a new system focal length.

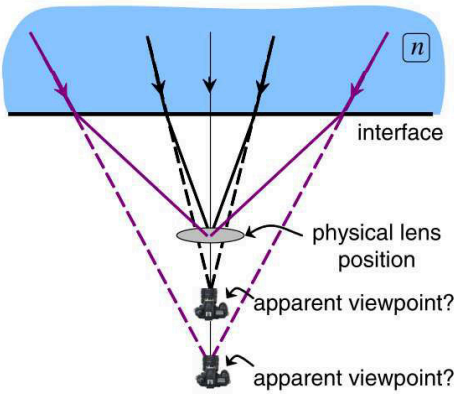

Figure 24: Non-SVP while looking through a flat interface. (TREIBITZ; SCHECHNER; SINGH, 2008)

The first possible solution is to consider the camera as axial (AGRAWAL et al., 2012), i.e., the focal point is variable with the light ray angle of incidence. This is a more physically accurate method, since each ray is traced following its actual path. However, in this model, new calibration parameters must be estimated, thus the calibration becomes more complex. Even though the camera is considered axial, all the rays still physically pass through the pinhole center point.

The underwater camera model used on the axial camera con-

sideration is as follows, shown in Figure 25. Considering a pinhole model camera watching a 3D point through n, perfectly flat windows, $i = 1, 2, ..., n$, with an angle between the camera axis and the window normal vector. Building the light path from the camera to the object points, the first ray is v_0 in the medium with refractive index μ_0, this ray reaches the first interface of refraction on the point q_0 with a distance d_0 from the pinhole center point. The ray is, then, refracted on the plane of refraction that contains the vector v_0 and the axis of refraction and the process is repeated for each layer. Thus, ray tracing the light ray from the camera is possible knowing the axis z_1,the distance between each interface d_i and each refraction index μ_i. These are the new calibration parameters, apart from the other camera parameters to be considered on this model. All these parameters can be obtained with only one underwater planar standard acquisition, for instance a check board. When considering a camera housing, watching the underwater environment through a flat window, some simplifications can be made. For example the glass width can be measured with a micrometer, which can have negligible errors or only one refraction can be considered (between water and air) instead of the two that actually happen (between water and glass and glass and air).

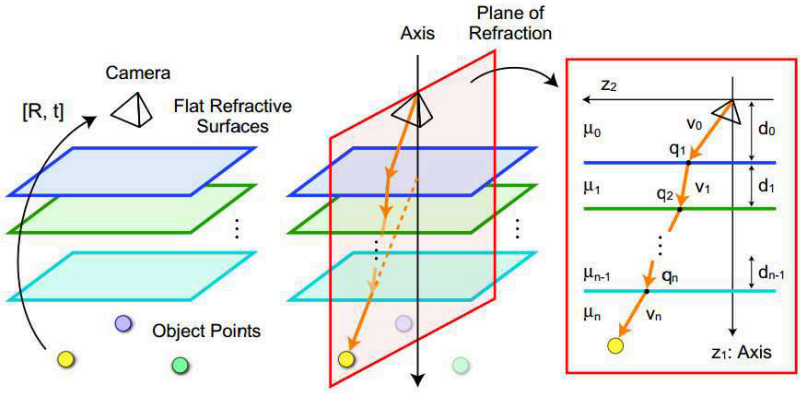

Figure 25: Multi-layer flat refractive geometry. (AGRAWAL et al., 2012)

A second possible way to consider the refraction during the measurement is to approximate the underwater distortion as a 2D radial distortion (KANG; WU; YANG, 2012). This technique can have good results in certain conditions where the refraction does not have a large influence, such as a smaller than 30° FOV. However, this also requires

a focal length approximation, since each light ray converges to a different point, depending on the angle of incidence. In this method, a set of 3D points is acquired on the measurement conditions, i.e. the camera mounted inside the housing and underwater. This set of points are used to calibrate the camera using the same methods used in-air. The results will be very different from the in-air ones, the focal length and the distortion coefficients will both be larger. This, then, requires a set of underwater acquisitions on the measurement environment.

Both methods have advantages and disadvantages. Mainly that the axial camera is more physically accurate, thus more flexible for different system configurations, but it is harder to implement than the SVP approximation. In this work the focus will then be the more physically accurate method, since the developed software will be applicable for different configurations.

3 UNDERWATER DEVELOPED SENSOR

The built LTS and the algorithms developed for measurement and calibration methods are described in this section. The designed LTS is optimized for underwater measurements using both the algorithms.

3.1 MECHANICAL DESIGN

The sensor was designed and was built by following the decisions described here. First, some design requirements are listed aiming at the oil and gas industry, then the system features to reach these goals are chosen and implemented in the built sensor.

3.1.1 Design Requirements

The sensor is aimed at the oil and gas industries need to verify underwater equipment. These procedures are essential to grant the whole safety and maintenance of the system. One of the most usual pieces of equipment are oil and gas ducts with a typical duct diameter of 300 mm.

Thus, the main LTS requirements are:

- The sensor must be designed to measure one fifth of a 300 mm diameter tube transversal section. This is a common procedure in the oil and gas industry to estimate the equipment condition.
- The final measurement uncertainty must be close to tenths of millimeters to gather the required object state.
- The distance from the measurement system to the surface of interest must ensure the equipment safety. Here, the considered distance is of at least 150 mm.
- The system must also be modular, to enable future changes in the measurement volume by changing the system baseline and triangulation angle.

The requirements are used to fulfill the equations used to model the LTS and decisions made during designing. The procedures and equations used during the process are described in the next section.

3.1.2 System Design

The system design consists of choosing the right system features to satisfy the design requirements and build the system in accordance with the safety rules. The LTS features to be chosen are triangulation angle and baseline. The hardware to be chosen is a, image sensor, a lens, a laser and laser line projection optics. Then, the housing must be designed to seal and fix the sensor components for underwater use. The final designed sensor is presented in Figure 26.

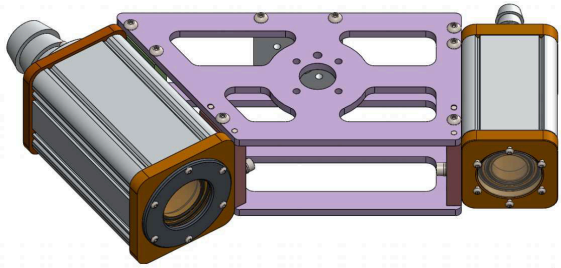

Figure 26: Designed sensor. Source: Author's own work

The first tests were made using a laser triangulation mathematical model. The triangulation angle, camera and lens choices were made based on this model. Using a water tank to simulate underwater measurements the base line was later adjusted to fulfill the requirements.

Three requirements were initially considered: measuring one fifth of a 300 mm diameter pipe transversal section, tenths of millimiters uncertainty sensor and the required distance from the sensor to the measured surface to allow the system safety. The uncertainty here is approximated as a sensor resolution, i.e. the mm variation per pixel. This is a reasonable initial approximation, because, even though the final uncertainty is bigger than the sensor resolution, the laser peak is detected with sub-pixel resolution.

The measuring of a 300 mm diameter tube in 5 divisions requires a minimum of 176.3 mm along the laser line, as shown in Figure 27.

To estimate the Y measurement range, the equation 2.11 is used. Then, the result is multiplied by the number of pixels in the corresponding Y direction. Because the Y resolution changes within the measurement volume, the stand-off was used.

The Equation 2.9 was used to estimate the LTS resolution on the Z direction.

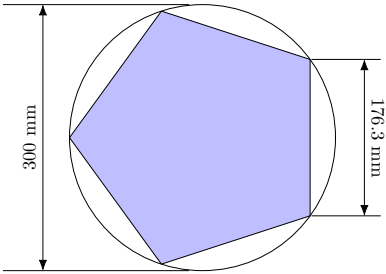

Figure 27: Inscribed pentagon side sized in a 300 mm diameter circle. Source: Author's own work

$$\delta Z = \frac{B \cos\theta_t f s_x}{(f \tan\theta_t - s_x B \cos\theta_t)^2} \delta u \tag{3.1}$$

The initial desired δZ is 0.2 mm per sensor pixel considered the image center. The first choices were the triangulation angle and the image sensor.

Triangulation angles can vary from 15° up to 80°, an initial estimate is, the bigger the angle, the smaller the measurement volume and consequently, better the resolution. Since the sensor is aimed at mid range measurements, the initial considered triangulation angle was 35°.

The selected camera must have a global shutter, because the whole laser line must be captured in the same moment. This way if the sensor is moving during a measurement, for example, attached to an ROV, the measurement results are not affected. The chosen camera resolution is 1.3 mega pixels as an array of 1280 pixel columns and 1024 pixel lines and a pixel size of 5.3 µm. This is also a camera with medium resolution among the machine vision cameras.

The baseline and focus were left as variables. The considered mid FOV lenses were 8 mm and 12.5 mm focal lengths. Another variable was the camera position in respect to the laser line: the laser line along the sensor line or the laser line along the sensor columns, which allow a bigger measurement length along the Z or Y directions, respectively.

The last requirement is the distance from the sensor to prevent accidents, the considered safety distance was of at least 150 mm from the beginning of the measurement volume. This distance can be geometrically approximated by drawing the current configuration. After applying the equations, and the geometrical approximation the 8 mm

lens could not reach the required Y range within the safety distance, so the 12.5 mm lens was chosen. The baseline was set, as a first approximation to 240 mm with the laser line along the sensor columns. The underwater influence was approximated to make the resolution 1.33 higher, i.e. a magnification of 1.33. After choosing the camera, the lens and the laser, the free variables are the triangulation angle and the baseline.

The FOV lens with the selected camera was obtained by positioning a graph paper at known distances from the lenses. The FOV was used to simulate the final measurement volume in a 3D model software, as shown in Figure 28. The desired Y direction distance along the laser and the object distance to the sensor, were also optimized during this procedure. The desired requirements were obtained with an adjustment to the baseline.

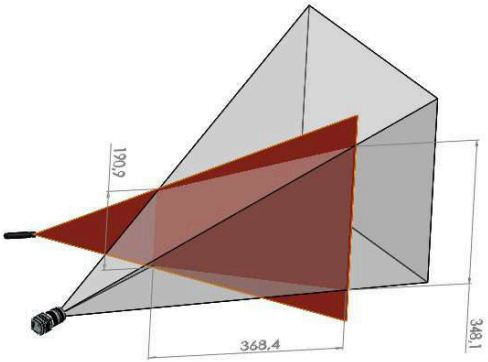

Figure 28: LTS 3D model optimization with in-air values. Source: Author's own work

Subsequently, the camera and laser were positioned outside of a water tank, shown in Figure 29, with an angled wall to reproduce the final sensor positioning. In this set-up, the baseline was finally chosen.

Consequently, the system equipment and characteristics that meet the desired requirements are shown in Tab. 1.

The next step is to build the sensor housing and positioning structure. The sensor consists of the camera module, the laser module and the positioning structure. The modules are positioned by two aluminum sheets and four parallel pins, two in each module. These aluminum sheets also have holes to mount possible systems for auxiliary

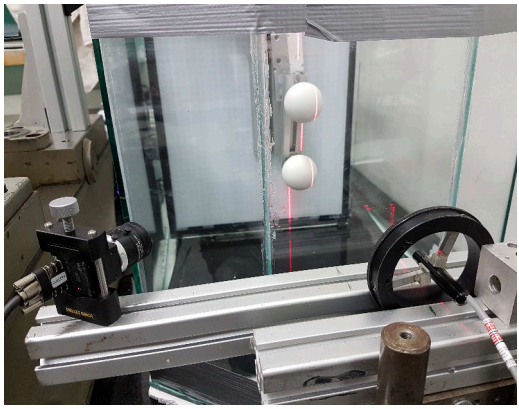

Figure 29: Angled wall water tank used in final evaluation. Source: Author's own work

Table 1: System parameters

Baseline	265 mm
Triangulation Angle	35°
Resolution	1.3 mega pixels
Pixel Size	5.5 μm
Orientation	Laser along the sensor columns
Focal length	12.5 mm

movement. This module set-up was chosen since, after changing the aluminum sheets, the modules can be positioned in different distances and angles, enabling a measurement volume variation.

The camera and laser were fully positioned without theoretical redundant alignments. Both the camera and the laser are positioned with respect to the superior aluminum sheet that permits the specified sensor baseline and triangulation angle.

The camera positioning and mounting is shown in Figure 30. The camera is fixed by two 'U shapes', but is only positioned by the superior 'U shape', which has a smaller inner space. The positioning features are: the plane behind the shape, one side of the 'U shapes'interior and the superior plane inside the 'U'. The 'U' shapes are fixed into another auxiliary element and positioned by three planes on this element. The

auxiliary element is then positioned on the lid by an internal cylinder, a plane and a positioning pin. The lid is positioned on the aluminum sheet support by a plane and two pins. The support is again positioned by two pins and a plane on the aluminum sheet.

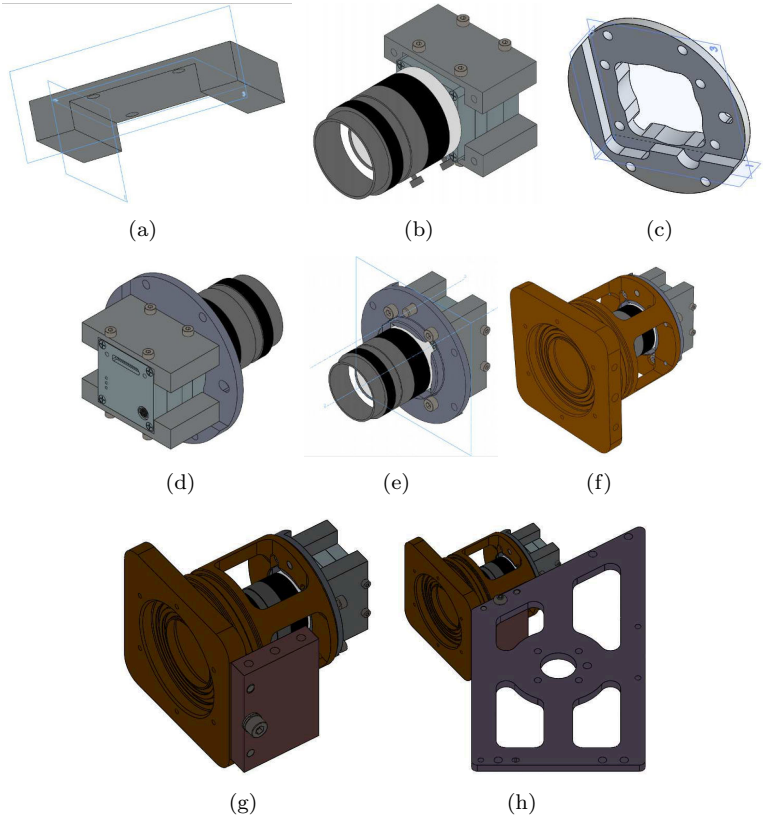

Figure 30: Camera positioning.(a) The positioning 'U' shape.(b) The camera fixed on the 'U' shapes. (c) The auxiliary fixing element positioning. (d) The camera mounted on the auxiliary element. (e) The auxiliary positioning element with respect to the lid. (f) The camera mounted on the lid. Source: Author's own work

The laser axis must be perpendicular to the window and coincident with the lid axis, this positioning is shown in Figure 31. The laser is fixed by a claw mechanism that is also centered in the window center. Then, the laser claw mechanism has an inside cylinder that fits

inside the front lid. Finally the laser lid is fixed to the aluminum sheet in the same way as the camera lid.

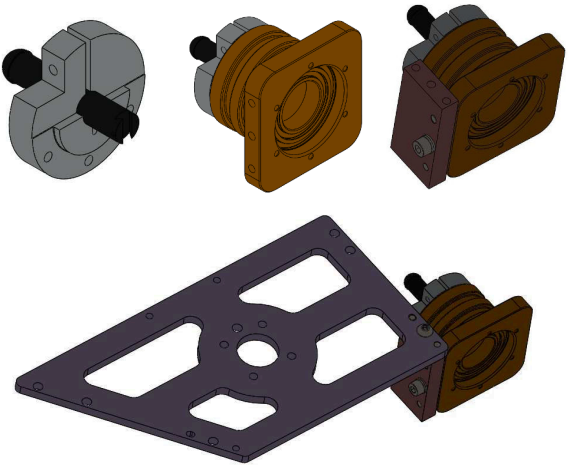

Figure 31: Laser positioning. Source: Author's own work

Besides the camera and laser positioning, the system is also fixed by another aluminum sheet under the sensor and the back lids also have additional holes for fastening the aluminum sheets.

The sensor, therefore, has four lids, two for each module. The lids have O-ring grooves for both the window and the housing. Additionally, the camera lid has reserved open space for the lens, so the focus and aperture can be adjusted while the camera is in the measurement position.

The modules housing are pneumatic cylinders and their sizes were selected by the camera and laser sizes. The camera has a diagonal length of 37.33 mm, models were created with each commercially available cylinder and the 63 mm diameter was chosen for the camera and the 50 mm for the laser.

The sensor sealing was made according to ISO 3601 (FLITNEY, 2011). The system uses two axial tandem O-rings in each window and two more radial O-rings in each of the frontal and back lids in the laser and camera modules. The aluminum tubes were measured in a CMM so that the O-ring squeeze is in the designed range. The camera FOV was used to optimize the spaces reserved for the O-rings.

The cables were connected to the inside of the housings by hoses

and sealed by hose barbs and O-rings on the flanges, as shown in Figure 32. Since the sensor is designed to dive to a maximum depth of 5 m, the hose barb is enough to grant the sealing. The hose diameter is 31.75 mm in the camera module and 12.7 mm in the laser module. The camera hose diameter is big enough to allow an USB 3.0 connector to move freely. The laser hose diameter is enough to insert the power supply cable.

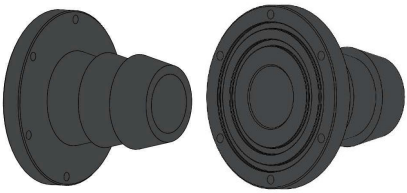

Figure 32: Details of the back flanges. Source: Author's own work

The windows were projected to resist a pressure differential of 1000 kPa aiming for the safety of the system.

Considering the window configurations shown in Figure 33.

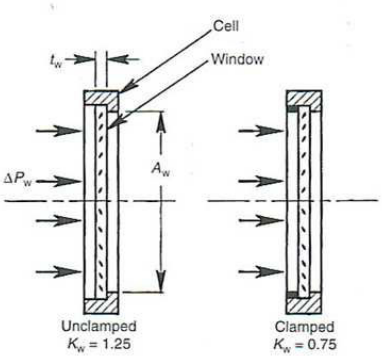

Figure 33: Clamped and unclassified configurations.(HARRIS, 1999)

Where t_w is the window thickness, A_w is the unsupported aperture diameter and ΔP_w is the pressure differential. The window thickness t_w must be greater than (HARRIS, 1999)

$$t_w = 0.5 A_w \left[K_w f_s \frac{\Delta P_w}{S_f} \right]^{1/2} \tag{3.2}$$

Where f_s is the safety factor (usually 4) and S_f is the fracture strength. Examples of fracture strength values are found in Figure 34.

Material	Strength (MPa)
Silicon carbide	600
Silicon nitride	600
Sapphire[32,33]	300-1000
Diamond (CVD‡)[34-40]	100-800
ALON	300
Spinel	190
Yttria (doped/undoped)	160
Silicon	120
MgF_2 (hot pressed)[41,42]	100-150
CaF_2 (single-crystal)[43]	100-150
Gallium phosphide§[44]	100-120
Gallium arsenide[45]	60-130
ZnS (standard)	100
ZnS (multispectral)	70
Germanium	90
SrF_2 (single-crystal)[43]	70-110
Fused silica	60
Zinc selenide	50

Figure 34: Window resistance values. (HARRIS, 1999)

The resulting thickness for the designed housing is 5.53 mm considering the camera module as the weaker window since it is the one with the larger unsupported aperture. Hence, the mounted window thickness is 6 mm, the closest available commercial thickness.

It is important to notice that the aluminum sheets are fixed to the front lid of each module and the auxiliary fixing element is used to fix the sheet to the lid, as shown in Figure 35. This way the sensor calibration can be made in the same configuration where the measurement will occur. Accordingly, adjustments, for example, in camera and laser focus, can be made in measurement positioning.

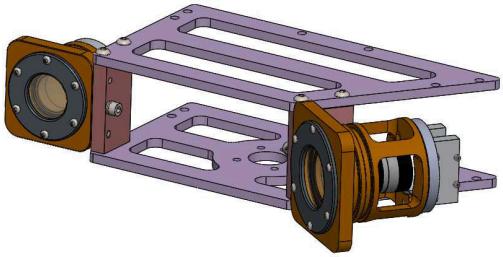

Figure 35: Sensor fixing during calibration. Source: Author's own work

The aluminum sheets also have auxiliary holes to mount the system into a moving system. The holes are to fit in a ABB robot. The sensor can be fixed from above or from behind, as shown in Figure 36.

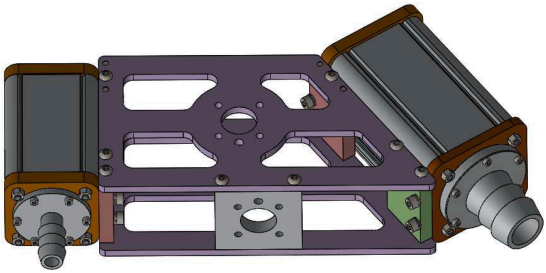

Figure 36: Back and superior fixing holes for auxiliary moving systems. Source: Author's own work

The system hardware, shown in Figure 37, is composed of a camera, a lens, a laser and line generator optics. The camera is a Ximea MQ013MG-E2, as mentioned, it has a resolution of 1.3 mega pixels and a pixel size of 5.3 µm. The lens is a Fujinon HF12.5HA-1B, which has a focal length of 12.5 mm and adjustable focus and aperture. The laser is a mini structured light laser diode modules with 635 nm wavelength, it uses line formation optics to project a line with an angle of aperture of 45° and has power of 7 mW.

(a) Camera (b) Lens (c) Laser

Figure 37: Hardware used to build the LTS. (MQ013MG-E2, 2017; HF12..., 2017; MINI..., 2017)

In Figure 38, the built LTS is shown.

The resulting β_s angle, to change the camera plane of focus to the laser plane is 87.9°, thus the Scheimpflug condition was not considered.

The sensor speckle limit resolution considering the f number of 4, at the standoff of 250 mm and the focal length of 12.5 mm is 16 µm.

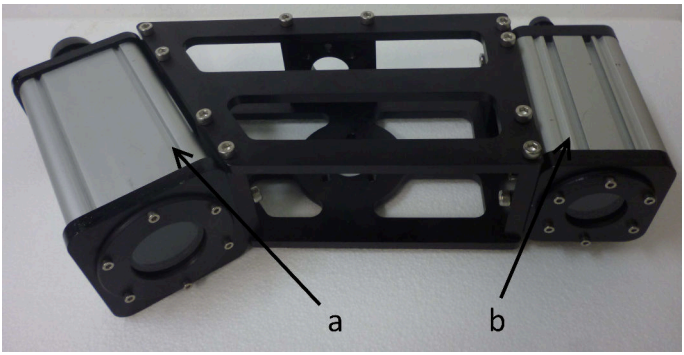

Figure 38: Built LTS. (a) is the camera module and (b) is the laser module. Source: Author's own work

3.1.3 Measuring Bench

The LTS must be displaced to build a dense point cloud. The sensor displacement and the new orientation must be known, allowing the point clouds concatenation. In this case, the displacement system is used both during calibration and measurement. The measuring bench allows this displacement to be controlled with good alignment between the elements.

The measuring bench is composed of a displacement system, a hydraulic system and a mounting structure. The complete measuring bench can be seen in Figure 39.

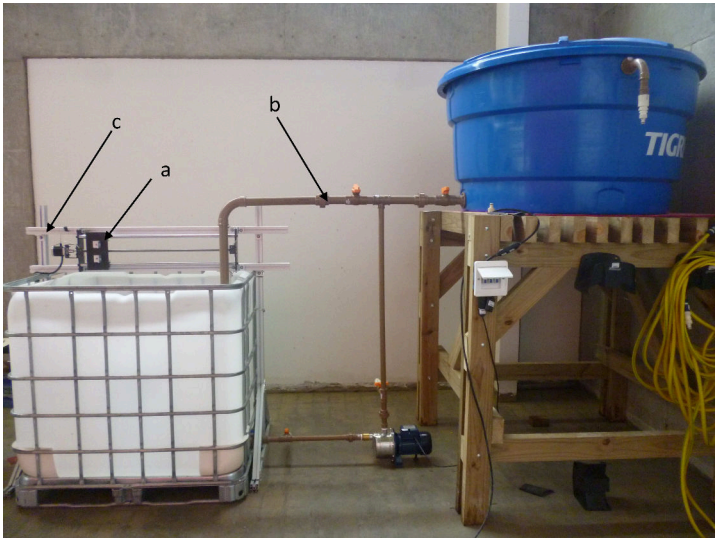

Figure 39: Complete measuring bench: displacement system (a), hydraulic system (b) and mounting structure (c). Source: Author's own work

In this work, the displacement system used to move the LTS is a linear slide, shown in Figure 41. It has a length of 750 mm and it is ball screw driven. The table is driven by the bipolar step motor AK23/15F6FN1.8, the driver AKDMP164.2A and a 42 V DC power source with 4 A peak current. The system is controlled by an Arduino micro controller which communicates via serialization with a personal computer. Apart from the slider control, the Arduino is also used along with a transistor to control the laser.

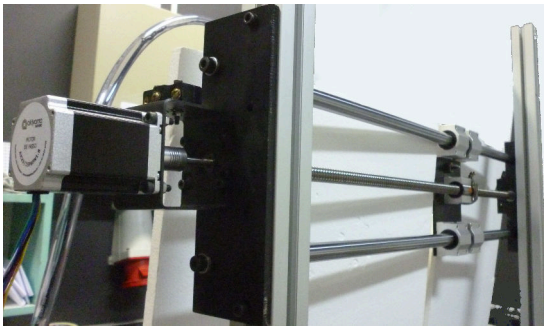

Figure 40: The linear slide and the motor. Source: Author's own work

The threaded rod has a lead of 5 mm and the motor has 400 steps per revolution, which results in a displacement resolution of 0.0125 mm per step. The driver allows motor micro steps, but this feature was not used.

The hydraulic system has a measuring tank, a storage tank, a water pump and the connecting pipes. During underwater measurements, the measure tank is filled by the height difference. Then, for in-air measurements, the water pump is turned on to drain out the water from the measurement tank to the storage tank. The system also has valves to allow a water change in the storage tank.

The mounting structure is made of aluminum profiles and it fastens the displacement table, the LTS and the calibration standard on the measuring tank. The LTS can be mounted facing downward (during measurement) or horizontally (during calibration). More details of both positions are presented in the evaluation section.

Figure 41: Mounting structure details. Source: Author's own work

3.2 DEVELOPED ALGORITHMS

Algorithms for measurement and calibration were developed. The calibration model considers one refraction between water and air to estimate the distance between the interface of refraction and the pinhole center. This distance, along with the camera calibration parameters, is used to ray trace the crossing between the laser peak ray with the laser plane.

To perform the underwater calibration, the system must already be calibrated in-air. The camera projection matrix, the distortion coefficients and the laser plane coefficients are, therefore, known.

First, the measurement procedure will be shown. This is a more logical sequence because the calibration procedure uses a very similar algorithm as the one used during measurement.

3.2.1 Measurement Algorithm

The measurement method considers a refraction, between air and water to back trace the crossing point between the detected laser peak and the laser plane. The following approximations where made :

- The camera is calibrated with the protective window, so the refraction on the glass is not considered, being approximated as a

radial distortion.

- The camera axis is considered normal to the refractive window, so that the axis of refraction is coincident with the camera axis.
- The laser plane is perpendicular to the protective window, therefore its refraction is not considered.

The influence of these considerations was also weighted during system evaluation.

The following model, shown in Figure 42, was used. A camera with pinhole center **C** and distance d from the interface of refraction observes a scene. An arbitrary ray **I** from the pinhole center reaches the interface of refraction at the point **q**, then it is refracted and transmitted on the **T** direction . The crossing between the ray **T** and the laser plane is the 3D point **X**.

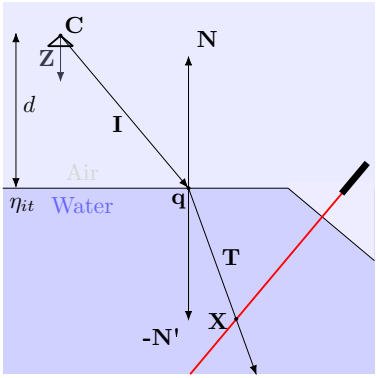

Figure 42: Measurement model. Source: Author's own work

The back trace from the image laser peak to the crossing with the laser plane is used to perform the measurement. During the ray tracing, each ray from each image line detected peak is refracted separately. The whole measurement procedure is shown in Figure 43. All the measurements are made in the CCS.

Before starting the measurement, the system must have all in-air parameters shown in Figure 43 estimated: distortion coefficients, camera matrix, window distance, refraction index and laser plane coefficients.

The first step is to acquire an image of the laser line projected on the surface of interest. After the acquisition, the image is corrected

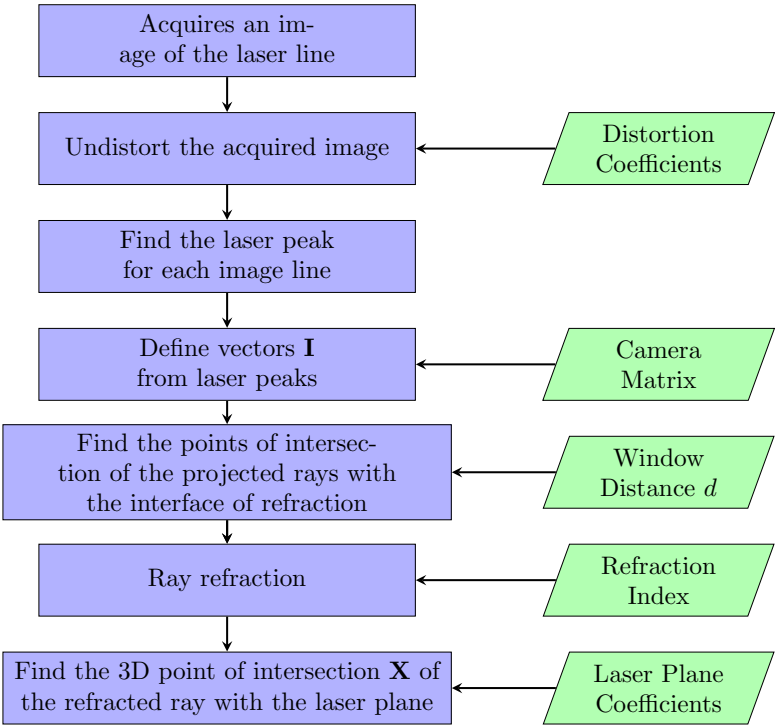

Figure 43: Measurement procedure. Source: Author's own work

from its distortion with the distortion coefficients. Then, the image is processed to extract the image coordinate containing laser peak for each image line. The first directional vector, v, which is also the incidence vector $\mathbf{I}$, is obtained from the laser peak pixel and the inverse of the intrinsic parameters matrix K

$$K^{-1}\mathbf{x} = \mathbf{I} \tag{3.3}$$

Where $\mathbf{x}$ is the laser peak pixel coordinate and $\mathbf{I}$ is the refraction incidence vector. After this, the point of intersection between this vector and the refractive window is found. The refractive window is considered a plane parallel to the image sensor, hence with normal, $\mathbf{N}$, pointing in the Z direction in CCS, i.e. with coordinates (0, 0, 1). The distance from the pinhole center to the refractive window is used in the interface of refraction plane equation. Point $\mathbf{p}_0$ is, then, $(0, 0, d)$ where d is the distance from the pinhole center to the window of refraction

and the plane equation for a point $\mathbf{p}$ on the window of refraction is

$$\mathbf{p} - (0, 0, d) \cdot \mathbf{N} = 0 \tag{3.4}$$

And the crossing between the line with direction $\mathbf{I}$ from the origin and the plane of refraction is the point q

$$\mathbf{q} = \frac{d}{\mathbf{I} \cdot \mathbf{N}} \mathbf{I} \tag{3.5}$$

The directional vector $\mathbf{I}$ is refracted on the plane of refraction and the transmitted ray $\mathbf{T}$ direction is given by the Eq. 2.18, presented again below

$$\mathbf{T} = \eta_{it}\mathbf{I} + (\eta_{it}(\mathbf{N} \cdot -\mathbf{I}) - \sqrt{(1 + \eta_{it}^2((\mathbf{N} \cdot -\mathbf{I})^2 - 1))}\mathbf{N} \tag{3.6}$$

The refracted ray has the equation

$$\mathbf{p}_t = k\mathbf{T} + \mathbf{q} \tag{3.7}$$

Where k is a scalar in $\mathbb{R}$.

The final step is to compute the crossing between the refracted ray equation and the laser plane, which is a plane with coefficients A, B, C, D.

Then, its normal direction vector is $\mathbf{N}_l = (A, B, C)$ and one point on the plane is $P_{0l} = (0, 0, -D/C)$ which results in the plane equation for a general laser plane point $\mathbf{P}_l$

$$(\mathbf{P}_l - \mathbf{P}_{0l}) \cdot \mathbf{N}_l = 0 \tag{3.8}$$

And the crossing between the laser plane and the transmitted ray $\mathbf{T}$ is

$$\mathbf{X} = \frac{(\mathbf{P}_{0l} - \mathbf{q}) \cdot \mathbf{N}_l}{\mathbf{T} \cdot \mathbf{N}_l} \mathbf{T} + \mathbf{q} \tag{3.9}$$

Resulting in the 3D point $\mathbf{X}$. The whole process is repeated for each image line forming the 3D point cloud for this sensor position. The point cloud is then transformed to the OCS, where the X vector is normal to the laser plane, to make the later concatenation of point clouds easier.

After this, the sensor is moved in the direction normal to the laser plane, which is the direction ± X in OCS, with a known displacement value. A new point cloud is obtained and, after the transformation to

OCS, the X coordinate is added to the displacement value, accomplishing the concatenation. The results from each acquisition are united, making the final three-dimensional point cloud.

Most of the parameters used during the measurements are obtained during camera calibration and laser calibration. The refraction index can be estimated with refractometers or some previous knowledge. So, the remaining window distance is the aim during the new developed calibration process.

3.2.2 Refraction Calibration Algorithm

The main idea of the refractive calibration algorithm is to measure some known underwater feature to optimize the window distance parameter used during measurement. Then, the proposed method consists, first, of a complete in-air calibration, i.e. intrinsic and extrinsic camera parameters, distortion coefficients and laser plane coefficients. After this calibration, some underwater acquisitions are taken from a standard with a known characteristic. The standard must have a feature possible to evaluate with only one line along the object, for example, here, the height between steps of a standard. The result of one acquisition of this object is shown in Figure 44. This underwater acquisition is used to estimate the distance from the pinhole center to the window of refraction, the distance d.

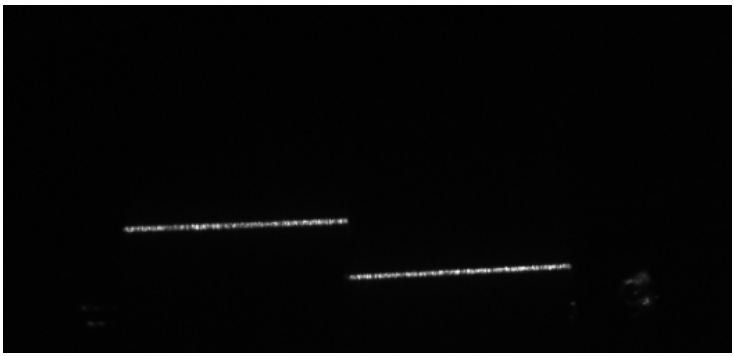

Figure 44: Resulting image from the step standard used during window distance calibration. Source: Author's own work

The measured 3D point depends on the refraction interface dis-

tance to the pinhole center and has an influence in the final result, as shown in Figure 45. However, this is a distance dependent on the camera and lens configuration, manufacturing tolerances and mechanical design, which is not always easy to estimate.

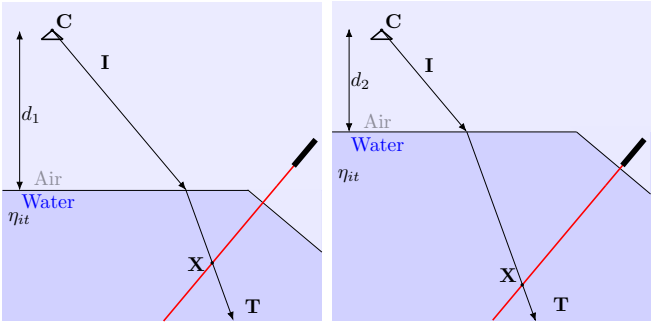

Figure 45: 3D point result for different window distances d. Source: Author's own work

The main objective of the proposed underwater calibration method is to estimate the window distance that minimizes the measurement error. The whole calibration procedure is shown in Figure 46.

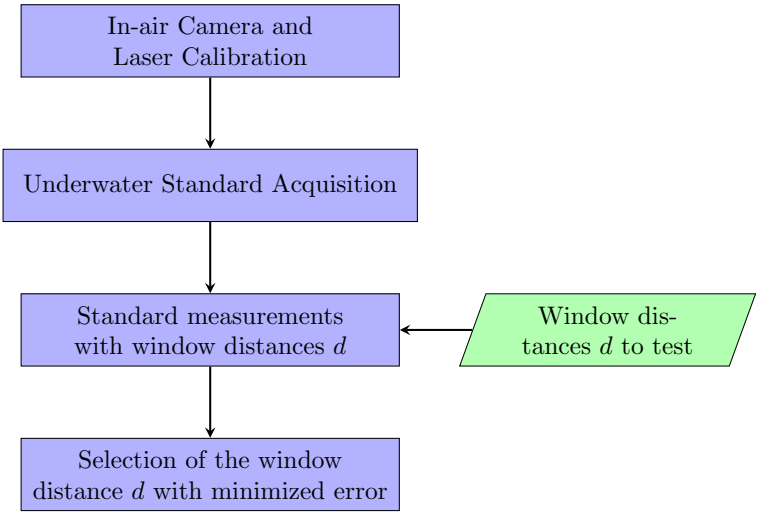

Figure 46: Calibration procedure. Source: Author's own work

After the in-air system calibration, some acquisitions of a standard are made underwater. This standard must allow the measurement of some feature with only one laser line. In the step case, it can have its height estimated. The standard must have the evaluated feature measured with a negligible uncertainty compared with the LTS uncertainty.

The underwater acquisition of the standard is used to repeat the whole measuring algorithm for a set of window distances to test. The result is a point cloud for each tested window distance with one acquisition. After this, the point cloud of each tested window is separately evaluated. In the step case, a line is adjusted in one of the steps and the mean distance from the points on the other step to the adjusted line is the measured height for this window distance. The calibration results is the window's distance d that minimized the evaluated error and is used in the measurement model.

4 SYSTEM EVALUATION

The evaluation was made using both the developed method and the polynomial adjustment, the latter used as a reference. All the results are compared with measurements in-air and underwater. The polynomial adjustment requires all the acquisitions to be underwater and the proposed method requires an in-air calibration and some underwater images of a standard in any non-previously known position.

To evaluate the system, two fixed calibrated spheres, a plane, a dummy head, welding beads and a 300 mm diameter pipe were measured. The spheres were calibrated with a CMM; the dummy head and the welding beads were measured with a commercial fringe projection system.

The camera and laser calibration were performed with a circle pattern standard. Additionally, to estimate the distance between the pinhole center and the refraction layer, a step standard was used, minimizing the measured height error.

The system mounting and alignments during calibration and acquisitions are also described in this section. They are aimed to minimize the influence of first order errors.

The calibration results using one or multiple underwater step images to estimate distance d were compared and the considerations of one or two refractions were evaluated. In the two refraction case the system was calibrated without the window and two refractions were considered during measurement.

After each calibration, in-air and underwater, the sensor is fixed in a linear displacement table to acquire images of all the described objects, then the images are processed using either the polynomial adjustment method or the proposed method.

4.1 EVALUATION OBJECTS

After all the calibrations, a few objects were measured to evaluate the system errors. They were measured both underwater and in-air using the polynomial method and the proposed method. Some objects were used to evaluate the LTS errors inside the various measurement volume portions, since the resolution varies along the volume, and other objects are presented as measurement examples.

The objects used to evaluate the method and the system, shown

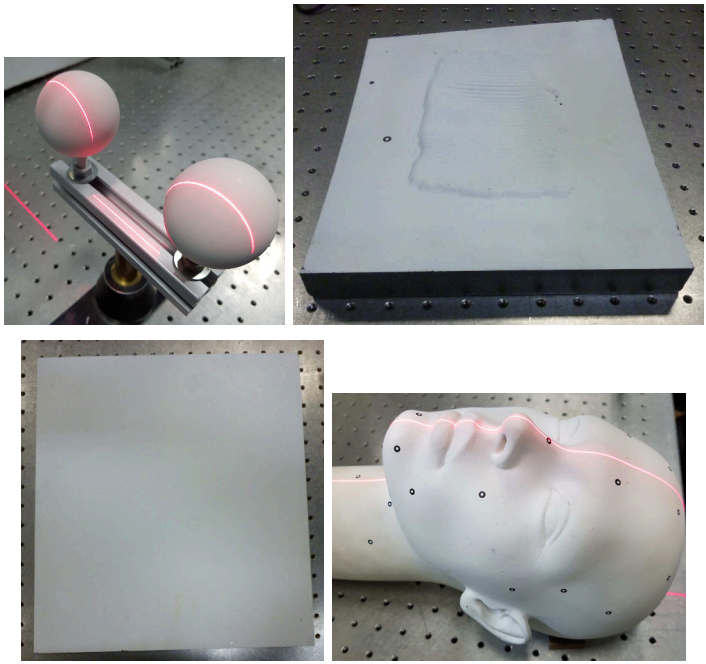

Figure 47: Evaluation objects: two fixed spheres, welding beads, a plane and a dummy head. Source: Author's own work

in Figure 47, are: two fixed spheres, welding beads, a glass plane, a dummy head and a 300 mm diameter PVC pipe. All the objects, except for the PVC pipe, were painted white to provide a diffuse surface.

The sphere standard is the main evaluation object, following the VDI/VDE 2634 (OPTISCHE..., 2000), the guidelines for optical 3D measuring systems. It consists of two fixed spheres with calibrated diameters and distance between its centers. The spheres were calibrated in a CMM. The sphere 1 has a diameter of 50.12 ± 0.01 mm and the sphere 2 has a diameter of 50.14 ± 0.01 mm. The distance between its centers is 99.18 ± 0.01 mm. The main parameters evaluated in the spheres with the LTS are the sphere spacing error (SSE) and the probing error (PE). The SSE is the difference between the measured distance between the spheres centers by the sensor and the calibrated distance. The range of distances, i.e. the peak and valley difference, of the measured 3D point to the fitted spheres is the PE. The standard deviation (STD) of these distances were also evaluated.

The spheres images were acquired in six positions along the measurement volume. Two acquisitions closer to the system, two on the stand-off and two on the end of the measurement volume. In each position, 38 images were taken, each moving the sensor 1 mm in the X direction in OCS.

The plane images were also taken closer to the system, on the stand-off and farther from the system. In each position, the plane was positioned both perpendicular to the laser plane and rotated around the Y axis at approximately 30°. Afterwards, 150 images were taken in each configuration. After each plane point cloud construction the range error (RE) is estimated. The RE is the range of distances, i.e. the peak and valley difference, of the measured 3D point to the best fitted plane. The standard deviation (STD) of these distances were also evaluated.

As measurement examples, a dummy head, welding bead and a 300 mm diameter PVC pipe were also measured with the presented techniques. The dummy head presents challenges for a LTS as the nose generates occlusions and discontinuities, which pose an obstacle to the laser peak search. The welding bead measurement aims to evaluate the capability of the sensor to measure smaller details. The 300 mm diameter pipe is the main sensor application objective as described in the mechanical design section. One set of acquisitions for each object on the stand-off was made.

4.2 CALIBRATION STANDARDS

The calibration standards are the objects used to calibrate the parameters needed during measurement. Two calibration standards were used for this work. One to calibrate the camera and the laser, a plane with a circle pattern, and the other to calibrate the refraction window distance, a step attached to a mirror.

To obtain the 3D points in the OCS used in the calibrations, a calibration standard, shown in Figure 48 is employed. The calibration standard consists of a glass plane with circular patterns. The OCS during calibration is defined by the circles and the table movement direction. Three circles at the center are black and define the origin and the X and Y coordinate directions. The Z coordinate is the vector normal to both directions. The X and Y variations in OCS are obtained from the distances between the circle centers, which were measured with a measuring microscope and are 9.375 mm in X direction and 9.372

mm in the Y direction. The Z coordinate was measured by known displacements of the linear slider.

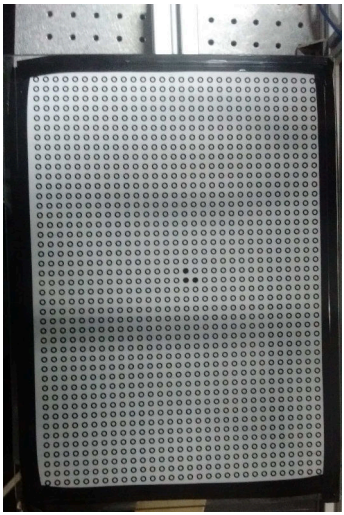

Figure 48: Calibration Standard. Source: Author's own work

The step, shown in Figure 49, is formed by glued steel parallelograms on a mirror. The distance between steps was measured in multiple positions with a microscope and a linear stage and has a height of 23.17 ± 0.02. The mirror is important to minimize the influence of a rotation around the X axis during the acquisition, which introduces a first order error in the step measurement.

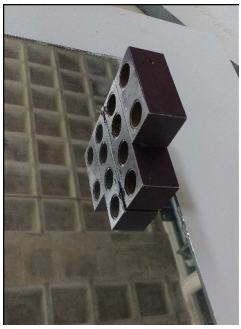

Figure 49: Step Standard. Source: Author's own work

While the step standard can be aligned using only the mirror, the circular pattern must be moved by the slider and properly aligned with respect to the LTS. This requires some calibration layouts, as well as a layout to adjust the lens and the laser.

4.3 CALIBRATION LAYOUT

The calibration layouts are the methods to mount and to align the planar standard and the LTS. Two calibration layouts were used: in the first, shown in Figure 50, the laser and camera are adjusted and in the second, shown in Figure 51, the planar standard images used during calibration are acquired.

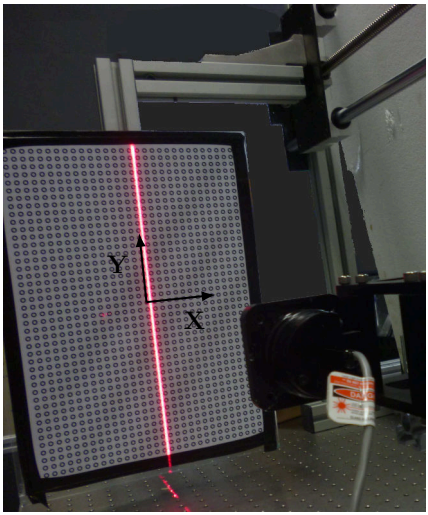

Figure 50: Calibration layout used to adjust the laser and the camera, also showing the OCS. Source: Author's own work

In the first layout, the laser focus and the camera aperture and focus are adjusted, since the sensor is without the housing. They are both adjusted with the standard at the standoff distance. The first step is to focus the laser, after this, both the camera focus and the aperture are adjusted. The aperture is set to fully open and the focus is adjusted, then the standard is moved to the end of the measurement volume and the aperture is closed up until the image is in focus. This allows the speckle to be as small as possible while the laser line is in

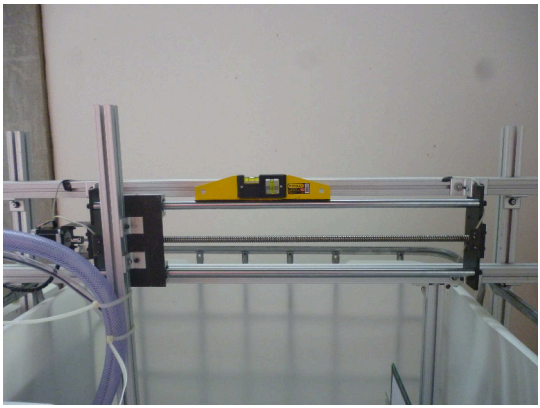

(a) Slide alignment

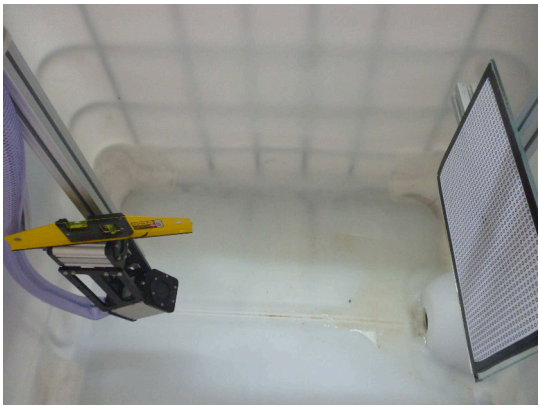

(b) LTS alignment

Figure 51: Calibration layout used to acquire the calibration images. First the table is aligned (a), then the LTS is aligned (b), both with a spirit level. Source: Author's own work

focus. Next, the laser is positioned perpendicularly to the top sensor fixing aluminum sheet, this element will be used as reference to fix the LTS later during measurement. Hence, the LTS is aligned with the linear slide movement direction.

In the second calibration layout, the calibration standard is fixed on the measuring tank mounting structure and the LTS is moved by the linear slide. The aim of this positioning is to minimize the error from the misalignment between the table movement direction and the Z coordinate from the LTS OCS.

The calibration standard is fixed on the aluminum structure with thick acrylic adhesive double sided tape and a square is used to align the standard with the profile. Then, the structure with the standard is fixed on the linear slider mounting structure.

A spirit level is used to align the laser with the table displacement during calibration.

The OCS used during calibration is based on the calibration standard. This coordinate system does not have the YZ plane on the laser plane. Later, during measurement, the OCS will be changed so that the X coordinate is mathematically perpendicular to the laser plane, i.e. the table displacement direction, thus minimizing the error from this misalignment. Although, even with these considerations, this misalignment will still be a source of uncertainty for the measurement result.

The calibration standard is moved 10 mm between acquisitions and there is is a wait time of 1 second, both underwater and in-air. The standard covered a distance of 300 mm in-air and 220 mm underwater in the Z direction.

4.4 ACQUISITION LAYOUT

In the acquisition layout, shown in Figure 52, all images used later during the measurement were acquired. Here, the LTS is moved by the linear slide and the measured object is fixed.

The OCS is defined so that the X direction is perpendicular to the laser plane. The LTS is aligned based on the linear slider with a spirit level, so the laser plane is perpendicular to the direction of movement. This results in a displacement vector close to the X direction, thus making the concatenation easier and more accurate.

During the measurements, the LTS is moved 1 mm between image acquisitions. To avoid error due to vibrations, there is a one second

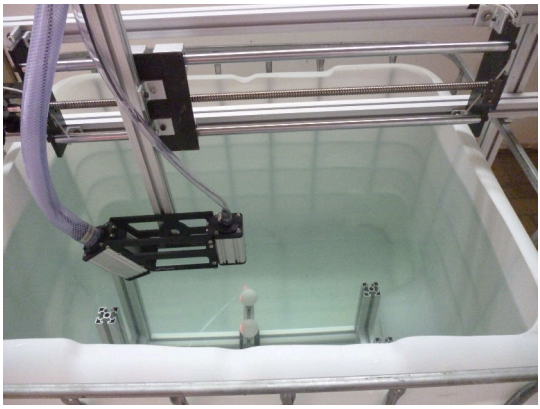

Figure 52: Acquisition layout. Source: Author's own work

wait after the movement. Then, the images are processed using either the polynomial adjustment or plane adjustment calibrations. The same positioning was used in all the acquisitions.

4.5 IMAGES PROCESSING

The image processing is an essential step during a LTS measurement and calibration. All the acquired images are processed to better find both the circle centers of the calibration standard and the laser peaks. Even though the image is separated in pixels, the aim of the image processing is to reach the sub-pixel level through image processing operations and interpolations.

The image processing to estimate the circles centers is shown in Figure 53. The following sequence of processing operations is applied: median filter with a size of 5 x 5 and 12th order, threshold with background correction, circle hole filling, elimination of particles on the border , removal of small particles and estimation of each ellipse center by the function IMAQ Fit Ellipse 2 in LabVIEW. The ellipses'center coordinates are used to find the circles with a black center on the original image and the coordinate system X and Y direction is built. Finally, the ellipse centers are given 3D coordinates using the real distance between centers in mm.

The laser peaks are estimated after a threshold with background correction and a 5 x 5 size low pass filter. Then, quadratic equations

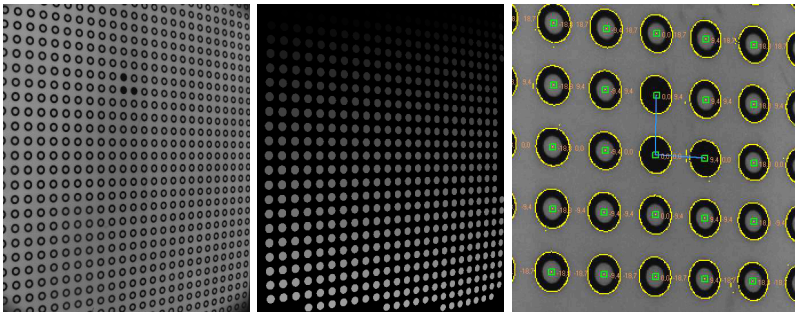

Figure 53: First, the original acquired image, then the processing result and the labels. Source: Author's own work

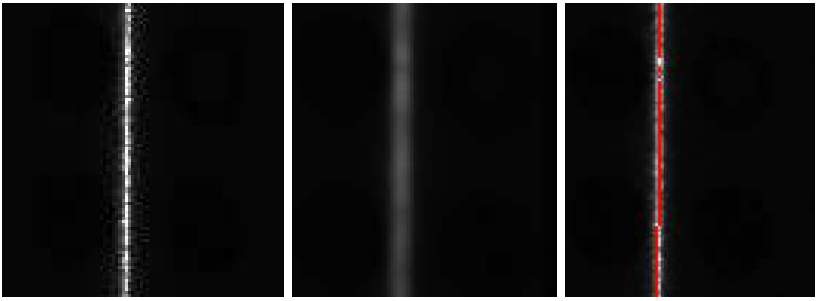

Figure 54: Laser image processing to peak search. First, the original image, then, the filter and the laser peak position (not shown with subpixel resolution). Source: Author's own work

are adjusted every few columns along the line being evaluated and the peaks are estimated. The process is shown in Figure 54.

The processing of circle centers is used as references to calibrate the camera and the laser. The processing of the laser peaks is used during both calibration and measurement. The detection of these features is an important source of uncertainty.

4.6 ACQUIRED IMAGES

The image acquisition process is a great source of uncertainty. Since the sensor must be displaced to create a dense point cloud, the

acquisition direction and the distance displaced by the slider are some of these sources. Some acquisition images are presented along with the sensor movement direction. All the presented images are still distorted.

The spheres were positioned in three different distances from the sensor, as shown in Figure 55, in-air and underwater.

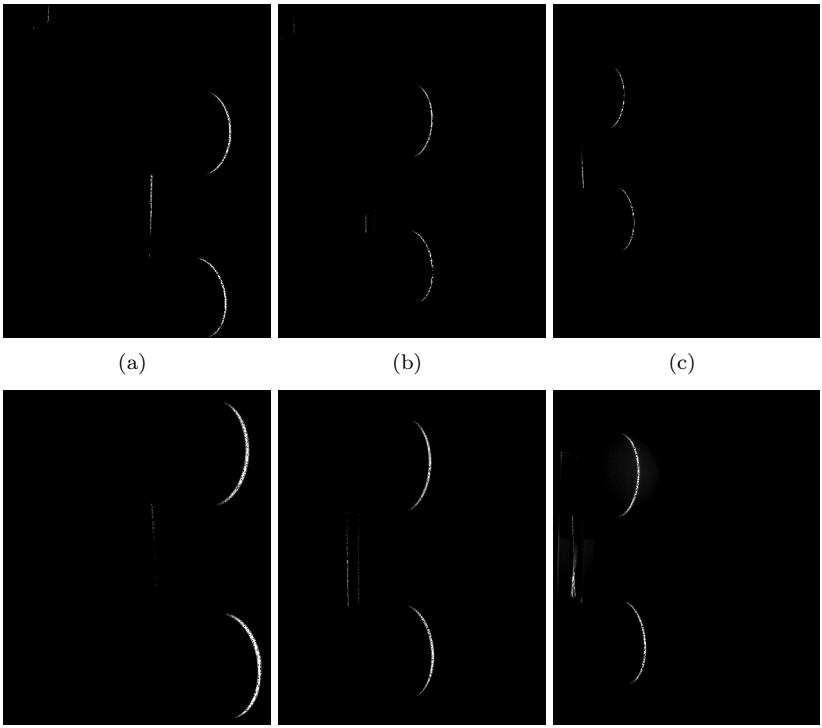

Figure 55: Sphere acquisitions.(a-c) images shown in-air. (d-f) images underwater. Respectively close to the system, on the stand off and farther from the system. Source: Author's own work

The plane, the dummy head, the welding beads and the PVC tube image examples are shown in Figure 56. The main difference between in-air and underwater images is the measurement volume. For example, the laser line is completely captured during underwater PVC tube measurement, but in-air, the line does not appear in all image lines.

The sensor movement direction for the sphere, the dummy head and the welding beads are presented in Figure 57. These are examples of meshes created by the LTS. The sensor movement direction aims to minimize the linear slider influence on the measurement result.

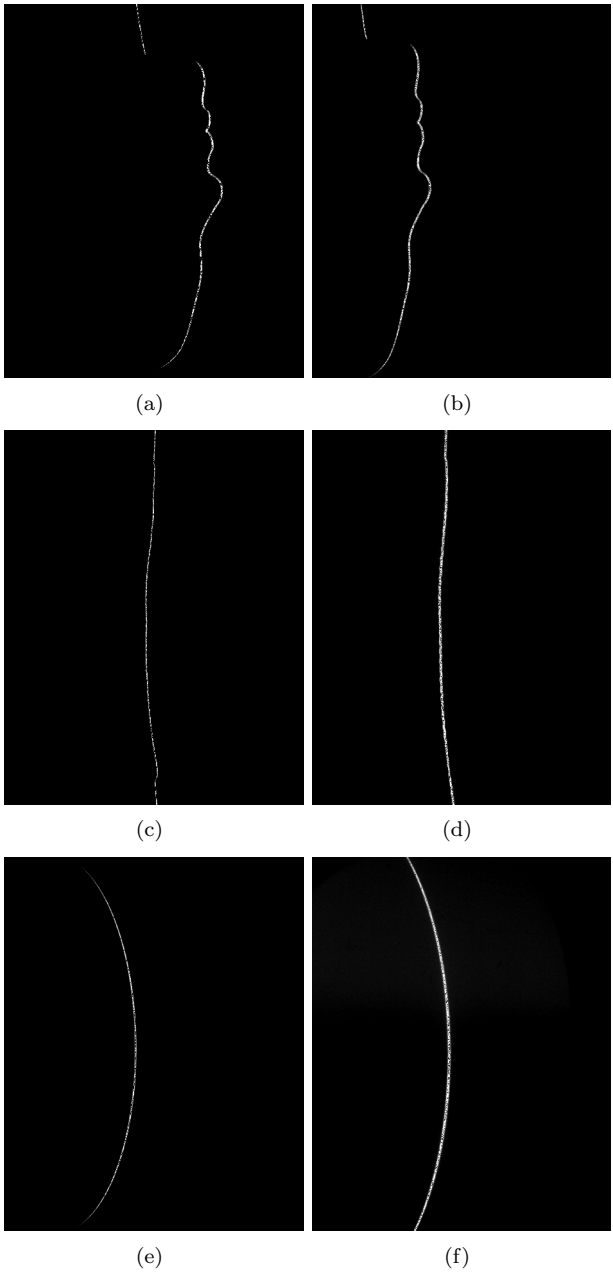

Figure 56: (a) (c) and (e) are in-air images. (b) (d) and (f) are underwater images. Respectively from the dummy head, the welding beads and the PVC tube. Source: Author's own work

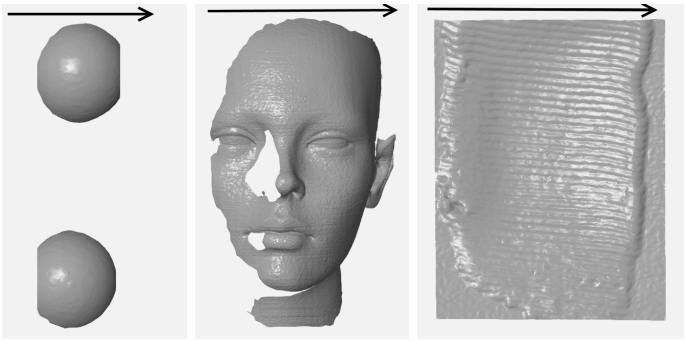

(a) Spheres (b) Dummy head (c) Welding beads

Figure 57: Sensor movement direction during acquisitions. Source: Author's own work

4.7 POLYNOMIAL CALIBRATION

As a comparison with the proposed method, a modeless calibration was also adopted. This is considered a reference method, because all the considerations made in the proposed method are absorbed during the polynomial adjustment.

The calibration with the polynomial equations were made in-air and underwater. For each line, two sixth-degree polynomials were fitted: one relating the laser peak column v with the Z coordinate Z(v) and another relating the Z coordinate with the Y coordinate Y(Z). After the laser peak detection, the detected column v is applied to the Z(v) equation and the resulting Z coordinate is applied to the Y(Z) equation. Resulting in the Z and Y coordinates for the detected peak. The process is repeated for each line.

These polynomial are, then, correlated with the image peaks detected from the acquisitions. The Z(v) polynomial equations have a mean residual of 0.06 mm in-air and underwater. The Y(Z) polynomial equations have a negligible mean residual error.

Examples of the adjusted polynomial equations are plotted in Figure 58 and Figure 59. The plotted polynomial equation are from one of the first image lines (top), from the image center (middle) and from one of last lines of the image (bottom). The distinct slope is noticeable when comparing the Z(v) polynomial equations in-air and underwater, because the underwater resolution is higher than in-air. The Y(Z) polynomial equations show the camera FOV in the Y direction as noted in the different equations for the top, middle and bottom image lines.

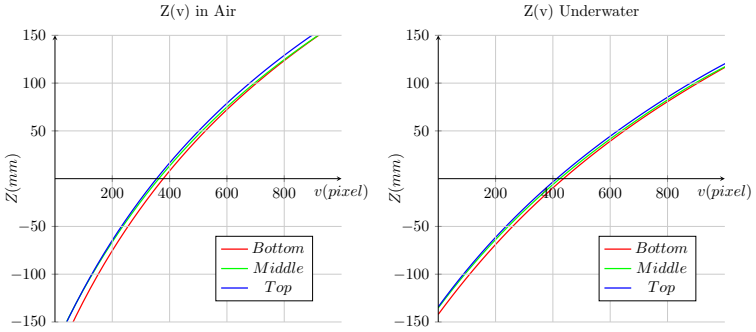

Figure 58: Z(v) polynomials examples from one of the top, middle and bottom image lines, in-air and underwater. Source: Author's own work

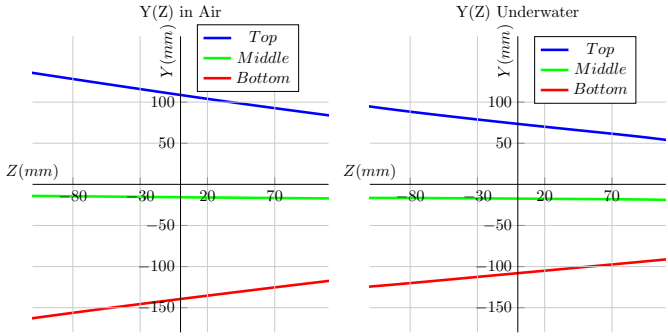

Figure 59: Y(Z) polynomials examples from one of the top, middle and bottom image lines, in-air and underwater. Source: Author's own work

4.7.1 Polynomial Adjustment Results

Polynomial equations were adjusted in-air and underwater and the results for each measured sphere standard and plane position are shown in Table 2 and in Table 3, respectively.

Table 2: Underwater sphere measurement errors for the polynomial adjustment. The worst measurement for each parameter is highlighted

	PE (mm)		STD (mm)		SSE (mm)	
	in-air	Underwater	in-air	Underwater	in-air	Underwater
Closer 1	**0.58**	**1.08**	**0.10**	**0.17**	0.17	0.06
Closer 2	0.47	0.97	0.09	**0.17**	0.33	0.15
Stand-off 1	0.57	0.86	**0.10**	0.14	0.28	0.02
Stand-off 2	0.49	0.69	0.08	0.13	0.32	0.11
Farther 1	0.50	0.66	0.09	0.11	0.20	**0.25**
Farther 2	0.48	0.65	0.08	0.11	**0.39**	0.10

The results in Table 2 show that the PE is bigger underwater and the SSE is bigger in-air. The underwater PE is worse in more distant acquisitions, one of the possible causes for this is the light absorption,

which intensifies the farther the object is. The SSE is expected to be bigger in-air, since the LTS has a better resolution underwater.

Table 3: in-air and underwater plane measurement errors for the polynomial adjustment.

	RE (mm)		STD (mm)	
	In-air	Underwater	In-air	Underwater
Closer	0.36	0.55	0.05	0.07
Closer Rotated	**0.80**	**0.75**	0.08	**0.12**
Standoff	0.34	0.62	0.06	0.10
Standoff Rotated	0.49	0.41	**0.09**	0.06
Farther	0.33	0.62	0.05	0.10
Farther Rotated	0.36	0.51	0.06	0.08

The measurement results using the polynomial method for the dummy head, welding beads and PVC tube are presented in Figures 60, 61 and 62. All the color map scales are presented with two standard deviations.

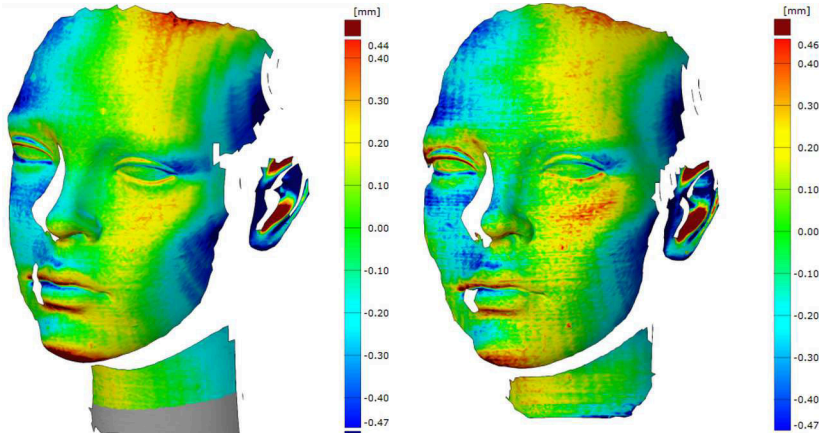

Figure 60: Dummy head measurements in-air and underwater using the polynomial adjustment. Source: Author's own work

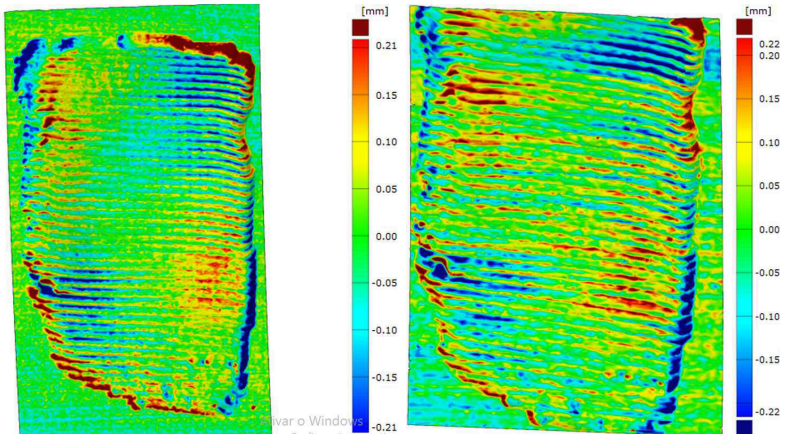

Figure 61: Welding bead measurements in-air and underwater using the polynomial adjustment. Source: Author's own work

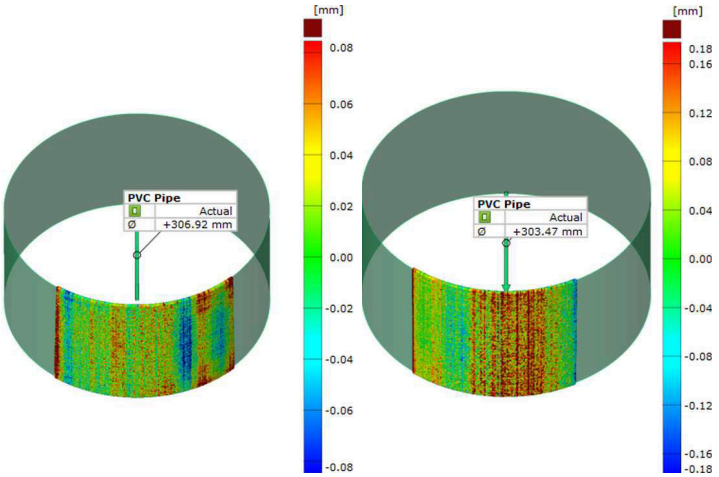

(a) In Air (b) Underwater

Figure 62: 300 mm diameter pipe measurements in-air and underwater with the polynomial method. Source: Author's own work

The dummy head and the welding beads have very similar color maps in-air and underwater. This shows the sensor's capability to measure more complex forms. These results are taken as a reference

for this LTS configuration.

4.8 PROPOSED CALIBRATION

The proposed calibration has two steps: one in-air sensor calibration and some underwater acquisitions. First, the intrinsic camera calibration parameters are obtained and, after, the window of refraction distance to the pinhole center is estimated.

In the first step, the same pattern used in the polynomial calibration is used for the in-air sensor calibration and the 3D points were obtained in the same way as in the polynomial calibration. First, the parameters of the camera are calibrated by direct optimization. Then, for each planar pattern position, an image with the laser turned on is also captured. For each laser peak in image coordinates, a line is projected using the camera matrix and its intersection with the planar standard at a known Z position is computed. The procedure is repeated for each standard position and a 3D point cloud that defines the laser plane is acquired.

After the in-air calibration, a step standard was used to calibrate the refractive window distance to the pinhole center. To validate this step, the nominal distance from the window to the pinhole center is approximated by combining the camera calibrated focal length, i.e., the distance from the camera imaging sensor to the lens focal point, and the distance between the sensor and the window from the mechanical design. The distance from the CMOS to the inner side window is 75.8 mm. According to the calibration, the focal length is 13.0 mm. Subtracting the mechanical distance by the focal length results in a refractive window distance of 62,8 mm.

4.8.1 Number of Underwater Images to Calibrate *d*

The estimated window distance variation with one and multiple images were also evaluated. Up to 9 images were used for comparison: three images from each position inside the measurement volume.

The results were compared using the spheres SSE parameter mean for all the acquired sphere positions. The step images were acquired closer to the sensor, at the stand-off and farther from the sensor. The resulting window distance when combining only the images from one region were also compared. The results are presented in Table 4.

Table 4: Relation between the number of step standard images used during calibration and the refractive window distance

	D (mm)	SSE (mm)	Mean (mm)	SSE (mm)
Closer	46.3	0.09	46.2	0.09
	42.6	0.23		
	46.2	0.09		
Stand-off	47.1	0.12	45.6	0.09
	43.4	0.17		
	45.6	0.09		
Farther	45.1	0.10	47.8	0.16
	47.8	0.16		
	47.9	0.16		

The result when using all the images is a window distance of 46.3 mm, this is a 16.5 mm difference from the mechanical project estimation. The regions closer to the sensor and at the standoff have the best estimation with the least number of images and three images from these areas were enough to estimate the optimal distance.

4.8.2 Refraction between Glass and Air

Although only one refraction is considered in the developed method, two refractions happen during acquisitions: between the air inside the camera housing and the window glass and between the glass and the water outside of the housing. One refraction approximation allows the system to be calibrated with the glass, bringing the calibration condition closer to the measurement condition.

To measure the influence of this consideration, the spheres were also measured considering two refractions. To consider this additional refraction, the system was calibrated without the glass and the window thickness was measured. The window thickness was measured with a micrometer in multiple positions and is 5.93 ± 0.02 mm. The glass index of refraction was considered 1.52.(III; VASCOTT, 2005)

The same nine step acquisitions used during the calibration with

refraction were used to calibrate the glass window distance, resulting in a new distance d of 40.7 mm.

After the calibrations, the spheres were measured and the results comparison are on Table 5.

Table 5: Measurement errors considering one or two refractions during spheres evaluation.

	One Refraction		Two Refractions	
	PE (mm)	SSE (mm)	PE (mm)	SSE (mm)
Closer 1	0.07	0.11	0.07	0.05
Closer 2	0.08	0.01	0.08	0.05
Stand-off 1	0.04	0.04	0.04	0.12
Stand-off 2	0.06	0.02	0.07	0.04
Farther 1	0.06	0.19	0.06	0.29
Farther 2	0.10	0.16	0.10	0.26
Mean	0.07	0.09	0.07	0.14

The mean resulting SSE for the one refraction consideration is 36% smaller than the two refraction consideration. A probable cause is the addition of new variables that were not optimized during calibration: the window thickness and the glass index of refraction. These may have been absorbed during the calibration in-air with the window.

4.8.3 Proposed Method Results

The final window distance after a calibration using all nine step standard images is 46.3 mm. The sphere and plane measurement errors are presented respectively in Table 6 and Table 7.

The results in Table 6 show a slightly worse PE underwater and a worse SSE in-air. These results are similar to the polynomial adjustment results.

The measurement results using the proposed method for the dummy head, welding beads and PVC tube are presented in Figures 63, 64 and 65. The color maps are scaled to two standard deviations.

Similar to the polynomial results the color map of the dummy

Table 6: Underwater sphere measurement errors for the proposed method. The worst measurement for each parameter is highlighted

	PE (mm)		STD (mm)		SSE (mm)	
	In-air	Underwater	In-air	Underwater	In-air	Underwater
Closer 1	0.48	**0.69**	**0.09**	0.12	0.29	0.08
Closer 2	0.47	0.66	0.08	**0.14**	0.34	0.06
Stand-off 1	**0.51**	0.51	0.08	0.12	0.35	0.09
Stand-off 2	0.44	0.51	0.08	0.11	**0.45**	0.02
Farther 1	0.47	0.46	0.08	0.10	0.35	**0.23**
Farther 2	0.36	0.48	0.07	0.10	0.44	0.18

Table 7: Underwater plane measurement errors for the proposed method.

	RE (mm)		STD (mm)	
	In-air	Underwater	In-air	Underwater
Closer	0.47	**0.62**	0.09	**0.10**
Closer Rotated	0.52	0.59	0.08	**0.10**
Standoff	0.37	0.50	0.07	0.09
Standoff Rotated	**0.62**	0.45	**0.12**	0.08
Farther	0.33	0.50	0.06	0.09
Farther Rotated	0.42	0.47	0.08	0.08

head and the welding beads are very related.

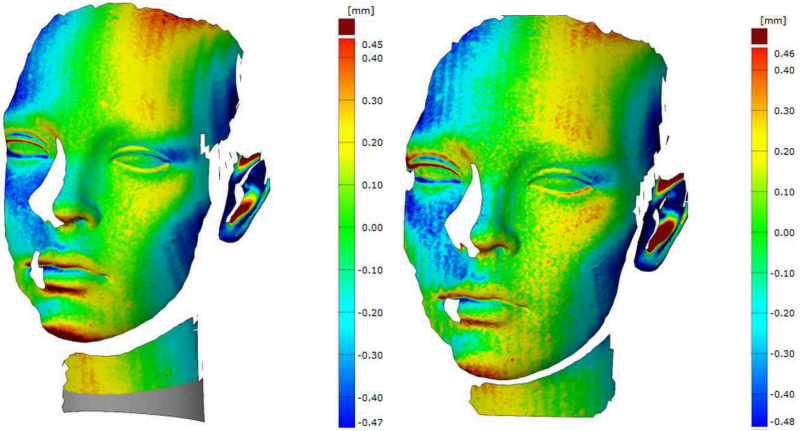

(a) In-air (b) Underwater

Figure 63: Dummy head measurements in-air (a) and underwater (b) with the proposed method. Source: Author's own work

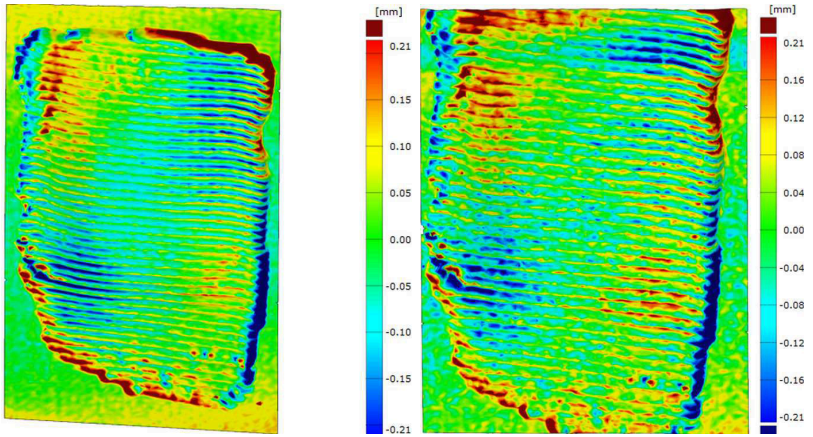

Figure 64: Welding bead measurements in-air and underwater using the proposed method. Source: Author's own work

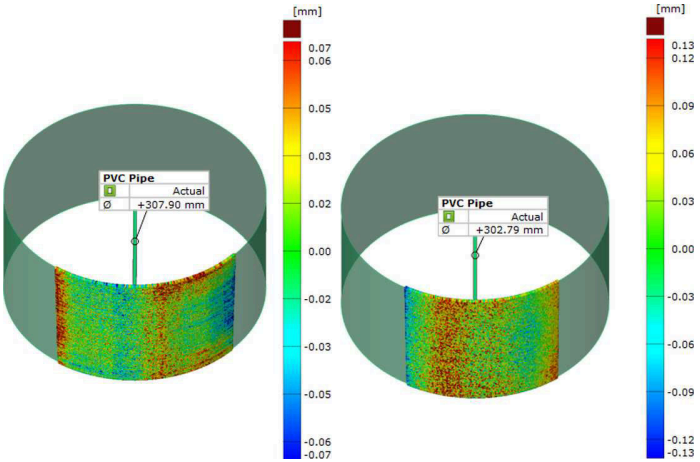

(a) In-air (b) Underwater

Figure 65: 300 mm diameter pipe measurements in-air (a) and underwater (b) with the proposed method. Source: Author's own work

4.8.4 Results Comparison

The full comparison is presented in Figure 66. The SSE and PE results are from the spheres. The values of the plane, dummy head, welding beads (WB) and the tube PE are one standard deviation for the measured object with the indicated method in the indicated environment.

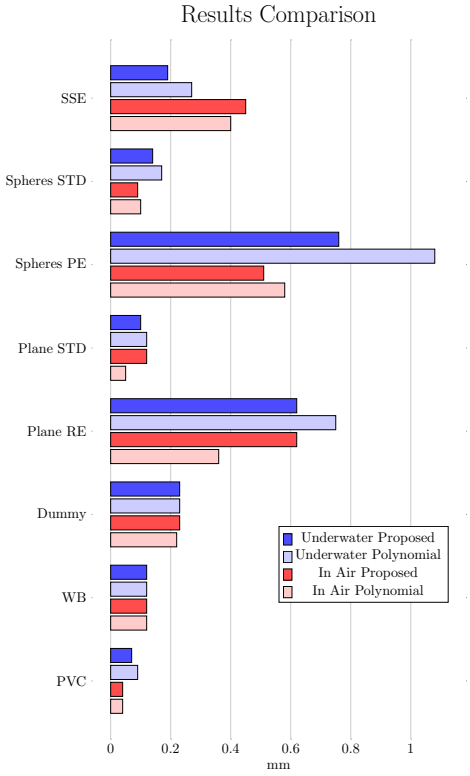

Figure 66: Comparison of all the measurement results. Source: Author's own work

The highest errors are presented in-air both with the polynomial and proposed methods while evaluating the SSE, however when comparing the probing error for all the objects, the in-air measurements had better results. Since in-air and underwater measurements have different measurement volumes, the errors must be compared with the

volume variation. In-air, the measurement length in the Z direction is 330 mm and underwater is 220 mm. The percent error related to the measurement volume is presented in Table 8, which is the division of the error by respective measurement length in the Z direction.

Table 8: Spheres spacing percent error

	In air		Underwater	
	Polynomial	Proposed	Polynomial	Proposed
SSE	0.12%	0.14%	0.12%	0.08%

Nevertheless, the uncertainty is more than two times higher in-air than underwater for the proposed method. This is hardly an acquisition error, since the probing error is lower in-air. One possible influence for this result for the proposed method is the underwater step acquisition and subsequent calibration, which adds another variable to minimize the errors. The residual errors from the camera and laser calibration are some of the strongest influences for these results.

4.8.5 Uncertainty Evaluation for the Proposed Method Underwater

To further evaluate the proposed method underwater, the sources of uncertainty contributions to the error were weighted. In the proposed method, the temperature affects the water index of refraction and the distance between the spheres' center. The sphere standard also has a calibration uncertainty and the developed system has a resolution between object displacement and pixel displacement. Finally, since six measurements were made, the repeatability of these measurements were evaluated.

- $\mathbf{U}_{\boldsymbol{\eta}}$ The temperature during measurements was considered to be $25 \pm 5°$C. This range causes an index of refraction variation of 1.3315 ± 0.0005 (BASHKATOV; GENINA, 2003). This causes a variation of 0.06 mm in the distance between center measurements at the stand-off. This source is considered to have a uniform distribution.

- $\mathbf{U}_{\boldsymbol{te}}$ This temperature range also causes a variation of ± 0.011 mm in the standard dimension due to thermal expansion. This source

is considered to have a uniform distribution.

- **Res** The resolution of a pixel in the Z direction at the stand-off distance is 0.22 mm. In the Z direction, the sensor has a subpixel peak search, therefore the effective resolution is considered to be one tenth of the pixel resolution.
- $\mathbf{U_{std}}$ The spheres were calibrated in a CMM, which has an uncertainty of $\pm 0.004mm$ for a 98.28 mm distance.
- **SSE** The repeatability was considered to be the standard deviation of the 6 measurements. The correction is the mean distance error.

All the results are shown in Table 9. C is the correction, U is the uncertainty, DoF is the degrees of freedom and total % in the source weight in the final value. The table was adjusted to 20°C since the measurements took place at the mean temperature of 25°C.

Table 9: Proposed method underwater uncertainty evaluation

Sources of Uncertainty				mm			
Symbol	Uncertainty	(±)	C	Distr.	u	ν	Total %
Uη	Index of refraction(η)	0.030	0.060	Uni.	0.017	∞	0.9%
U_{te}	Standard Expansion	0.010	0.011	Uni.	0.006	∞	0.1%
Res	Resolution	0.011	-	Uni.	0.006	∞	0.1%
U_{std}	Standard Calibration	0.002	-	Norm.	0.002	∞	-
SSE	Sphere Spacing Error	0.110	0.040	Norm.	0.110	5	37.6%
PE	Probing Error	0.140	-	Norm.	0.140	∞	61.2%

The combination of these sources results in 35 degrees of freedom. The expanded uncertainty is ± 0.37 mm and the combined correction is +0.11 mm resulting in a maximum error of ± 0.48 mm.

The cylindricity of the PVC tube and the real diameter were not evaluated with another system. Therefore, the obtained diameters cannot be compared with a calibrated value.

Overall, the proposed method and the polynomial adjustment method have very close underwater measurement uncertainties, but the proposed method has the advantage of fewer underwater acquisitions, besides being more physically accurate.

4.8.6 Y Direction Measurement Length

The minimum measurement length in the Y direction which allows five measurements to cover a 300 mm diameter tube is 176.3 mm. To confirm this designed LTS capability, the 300 mm diameter PVC tube was measured at the stand-off distance. The result is shown in Figure 67, which shows a length of 185.27 mm.

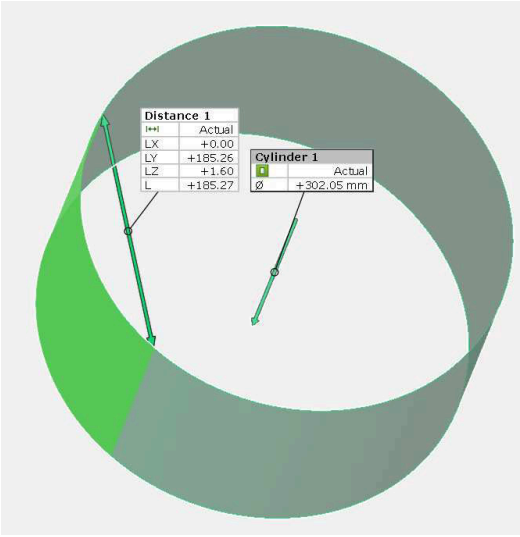

Figure 67: Y direction measurement volume. Source: Author's own work

5 CONCLUSIONS

In this work, a laser triangulation sensor (LTS) for underwater measurements was built aiming to fulfill the oil and gas industry's need to measure underwater equipment. The main objective was to measure a 300 mm diameter pipe with an uncertainty of half millimeter. The sensor was then built and two algorithms for calibration and measurement were developed and evaluated by multiple object measurements.

The sensor characteristics are: a lens focal length of 12.5 mm, 265 mm baseline, 35° triangulation angle, the measurement length in the Z direction starts at 200 mm from the sensor and goes up to 420 mm and at the stand-off, the laser line measures 184 mm. This permits the measurement of one fifth of a 300 mm diameter tube transversal section and a safety distance from the object of interest. It is also modular, allowing a measurement volume change by replacing the positioning sheets.

Two methods for calibration and measurement with LTS underwater were compared: the polynomial equation adjustment and a proposed two step method.

The polynomial adjustment is based on a correlation between the detected laser peak with the real 3D point. This requires a full underwater calibration with know standard displacements, since multiple non-planar 3D points are required.

The second, proposed method requires an in-air calibration and some underwater acquisitions of a step pattern. These underwater acquisitions are used to calibrate the window of refraction distance from the camera pinhole center, thus allowing the ray tracing from the camera to the laser plane, resulting in a measured 3D point.

The methods were evaluated by measuring multiple objects resulting in both having very similar underwater results. A standard with two spheres with calibrated distance between centers was the main evaluated object. After six acquisitions, both methods had a mean underwater distance between their centers error of 0.08 mm along the measurement and the proposed method had a maximum error of 0.48 mm. Apart from the spheres, multiple objects with varying shapes were measured having very similar results for both in air and underwater.

When comparing the in-air and underwater results, both methods also had similar results: better probing errors in-air, but better sphere spacing errors underwater. One cause for this effect is the measurement volume variation, since the measurement volume is smaller

underwater, leading to a higher resolution. Another probable cause for this result considering the proposed method is the additional images used during underwater calibration.

Ultimately, the designed sensor and the algorithms have proven to be suitable for the designed application. The proposed method accurately performs the ray tracing being applicable in other configurations.

5.1 FUTURE WORKS

Both the system and algorithms still have room for improvement.

Considering the proposed method, more parameters can be calibrated in situ within the underwater acquisition, such as the water index of refraction, lowering the sources of uncertainties from this estimation.

The step standard itself can be improved, because the built quality influences the refraction window distance estimation. A standard with a small parallelism error between the two steps may result in a more reliable estimation and may not need several images to grant the optimum distance.

The sensor can be mounted to a displacement system such as an ROV and algorithms of integration between the ROV locating system can be developed resulting in an out-of-laboratory measurement.

Additionally, since the sensor is modular, new configurations of the baseline, lens, camera, laser and triangulation angle can be tested for further evaluations.

REFERENCES

AGRAWAL, A.; RAMALINGAM, S.; TAGUCHI, Y.; CHARI, V. A theory of multi-layer flat refractive geometry. In: *Computer Vision and Pattern Recognition (CVPR), 2012 IEEE Conference on*. [S.l.: s.n.], 2012. p. 3346–3353. ISSN 1063-6919.

BASHKATOV, A. N.; GENINA, E. A. Water refractive index in dependence on temperature and wavelength: a simple approximation. In: INTERNATIONAL SOCIETY FOR OPTICS AND PHOTONICS. *Saratov Fall Meeting 2002: Optical Technologies in Biophysics and Medicine IV*. [S.l.], 2003. p. 393–395.

BESL, P. J. Active, optical range imaging sensors. *Machine vision and applications*, Springer, v. 1, n. 2, p. 127–152, 1988.

BIANCO, G.; GALLO, A.; BRUNO, F.; MUZZUPAPPA, M. A comparative analysis between active and passive techniques for underwater 3d reconstruction of close-range objects. *Sensors*, Multidisciplinary Digital Publishing Institute, v. 13, n. 8, p. 11007–11031, 2013.

BLUEVIEW BV5000 Harbor Scan. 2017. `https://www.youtube.com/watch?v=MWL3mBOUk-I`. Accessed: 2017-04-05.

BLUVIEW 3D Multibeam Scanning Sonar. 2017. `http://www.blueview.com/products/3d-multibeam-scanning-sonar/3/`. Accessed: 2017-04-05.

BROWN, D. C. Close-range camera calibration. *PHOTOGRAMMETRIC ENGINEERING*, v. 37, n. 8, p. 855–866, 1971.

BRUNO, F.; BIANCO, G.; MUZZUPAPPA, M.; BARONE, S.; RAZIONALE, A. Experimentation of structured light and stereo vision for underwater 3d reconstruction. *ISPRS Journal of Photogrammetry and Remote Sensing*, Elsevier, v. 66, n. 4, p. 508–518, 2011.

BUSCHINELLI, P. D.; MATOS, G.; PINTO, T.; ALBERTAZZI, A. Underwater 3d shape measurement using inverse triangulation through two flat refractive surfaces. In: IEEE. *OCEANS 2016 MTS/IEEE Monterey*. [S.l.], 2016. p. 1–7.

CACCIA, M. Laser-triangulation optical-correlation sensor for rov slow motion estimation. *IEEE Journal of Oceanic Engineering*, IEEE, v. 31, n. 3, p. 711–727, 2006.

CHANTLER, M. J.; CLARK, J.; UMASUTHAN, M. Calibration and operation of an underwater laser triangulation sensor: the varying baseline problem. *Optical Engineering*, International Society for Optics and Photonics, v. 36, n. 9, p. 2604–2611, 1997.

CHOOSING a 3D vision system for automated robotics applications. 2017. `http://www.vision-systems.com/articles/print/volume-19/issue-11/features/choosing-a-3d-vision-system-for-automated-robotics-applications.html`. Accessed: 2017-04-05.

CODAOCTOPUS Sound Underwater Inteligence. 2017. `http://www.codaoctopus.com/product-list/3d`. Accessed: 2017-04-05.

COIRAS, E.; PETILLOT, Y.; LANE, D. M. Multiresolution 3-d reconstruction from side-scan sonar images. *IEEE Transactions on Image Processing*, IEEE, v. 16, n. 2, p. 382–390, 2007.

COMPACT laser scanner for profile transmission. 2017. `http://www.micro-epsilon.com/2D_3D/laser-scanner/scanCONTROL-compact/`. Accessed: 2017-04-05.

CRISP real-time 3D sonar imagery. 2017. `http://www.codaoctopus.com/products/use`. Accessed: 2017-04-05.

DEY, P. K.; OGUNLANA, S. O.; NAKSUKSAKUL, S. Risk-based maintenance model for offshore oil and gas pipelines: a case study. *Journal of Quality in Maintenance Engineering*, Emerald Group Publishing Limited, v. 10, n. 3, p. 169–183, 2004.

DIVISION, U. of California (1868-1952). Division of W. R. S. D.; DIVISION, C. U. D. of W. R. S. D.; ECKART, C. *Principles of Underwater Sound*. Research Analysis Group, Committee on Undersea Warfare, National Research Council, 1946. (Summary technical report of the National Defense Research Committee: Summary technical report of Division 6, NDRC). <https://books.google.com.br/books?id=9kQrAAAAYAAJ>.

DORSCH, R. G.; HÄUSLER, G.; HERRMANN, J. M. Laser triangulation: fundamental uncertainty in distance measurement.

Applied Optics, Optical Society of America, v. 33, n. 7, p. 1306–1314, 1994.

DRAP, P.; SEINTURIER, J.; SCARADOZZI, D.; GAMBOGI, P.; LONG, L.; GAUCH, F. Photogrammetry for virtual exploration of underwater archeological sites. In: *Proceedings of the 21st international symposium, CIPA*. [S.l.: s.n.], 2007. p. 1e6.

FLITNEY, R. K. *Seals and sealing handbook*. [S.l.]: Elsevier, 2011.

GAN, Z.; TANG, Q. *Visual Sensing and Its Applications: Integration of Laser Sensors to Industrial Robots*. Zhejiang University Press, 2011. (Advanced topics in science and technology in China). ISBN 9787308080514. <https://books.google.com.br/books?id=nmYemwEACAAJ>.

GIBSON, R.; ATKINSON, R.; GORDON, J. A review of underwater stereo-image measurement for marine biology and ecology applications. *Oceanography and marine biology: an annual review*, CRC Press, v. 47, p. 257–292, 2016.

GLASSNER, A. S. (Ed.). *An Introduction to Ray Tracing*. London, UK, UK: Academic Press Ltd., 1989. ISBN 0-12-286160-4.

GUO, Y. 3d underwater topography rebuilding based on single beam sonar. In: IEEE. *Signal Processing, Communication and Computing (ICSPCC), 2013 IEEE International Conference on*. [S.l.], 2013. p. 1–5.

HARRIS, D. C. *Materials for infrared windows and domes: properties and performance*. [S.l.]: SPIE press, 1999.

HARTLEY, R. I.; ZISSERMAN, A. *Multiple View Geometry in Computer Vision*. Second. [S.l.]: Cambridge University Press, ISBN: 0521540518, 2004.

HF12.5HA-1B. 2017. `http://www.fujifilmusa.com/products/optical_devices/machine-vision/2-3-15/hf125ha-1b/`. Accessed: 2017-04-05.

HORNER, D.; MCCHESNEY, N.; MASEK, T.; KRAGELUND, S. *3D Reconstruction with an AUV Mounted Forward-Looking Sonar*. [S.l.], 2009.

III, T. P. S.; VASCOTT, T. *High temperature glass melt property database for process modeling*. [S.l.]: Wiley-American Ceramic Society, 2005.

JI, Z.; LEU, M.-C. Design of optical triangulation devices. *Optics & Laser Technology*, Elsevier, v. 21, n. 5, p. 339–341, 1989.

JI, Z.; LEU, M.-C. Design of optical triangulation devices. *Optics & Laser Technology*, Elsevier, v. 21, n. 5, p. 339–341, 1989.

JORDT, A. *Underwater 3D reconstruction based on physical models for refraction and underwater light propagation*. [S.l.]: Citeseer, 2014.

KANG, L.; WU, L.; YANG, Y.-H. Experimental study of the influence of refraction on underwater three-dimensional reconstruction using the svp camera model. *Appl. Opt.*, OSA, v. 51, n. 31, p. 7591–7603, Nov 2012. <http://ao.osa.org/abstract.cfm?URI=ao-51-31-7591>.

LOURAKIS, M. I. A brief description of the levenberg-marquardt algorithm implemented by levmar. *Foundation of Research and Technology*, v. 4, n. 1, 2005.

MASSOT-CAMPOS, M.; OLIVER-CODINA, G. Optical sensors and methods for underwater 3d reconstruction. *Sensors*, Multidisciplinary Digital Publishing Institute, v. 15, n. 12, p. 31525–31557, 2015.

MCLEAN, J. W. High-resolution 3d underwater imaging. In: INTERNATIONAL SOCIETY FOR OPTICS AND PHOTONICS. *SPIE's International Symposium on Optical Science, Engineering, and Instrumentation*. [S.l.], 1999. p. 10–19.

MIKS, A.; NOVAK, J.; NOVAK, P. Analysis of imaging for laser triangulation sensors under scheimpflug rule. *Optics express*, Optical Society of America, v. 21, n. 15, p. 18225–18235, 2013.

MINI Structured Light Laser Diode Modules. 2017. `https://www.edmundoptics.com/lasers/laser-diode-modules/mini-structured-light-laser-diode-modules/2273`. Accessed: 2017-04-05.

MQ013MG-E2. 2017. `https://www.ximea.com/en/products/usb3-vision-cameras-xiq-line/mq013mg-e2`. Accessed: 2017-04-05.

NAIDU, D.; FISHER, R. B. A comparative analysis of algorithms for determining the peak position of a stripe to sub-pixel accuracy. In: *BMVC91*. [S.l.]: Springer, 1991. p. 217–225.

NEWTON, I.; BALDWIN, R.; FRYER, J. Underwater photogrammetry. *Non-Topographic Photogrammetry*, American Society for Photogrammetry and Remote Sensing: Bethesda, MD, USA, p. 147–166, 1989.

OFFSHORE Laser Scanning for Asset Management. 2017. `https://www.2grobotics.com/offshore/`. Accessed: 2017-04-05.

OPTISCHE 3D-Messsysteme: VDI-VDE-Handbuch Meßtechnik. Bildgebende Systeme mit flächenhafter Antastung : VDI-VDE 2634, Blatt 2 Entwurf. Blatt 2. 2634,2E. Beuth, 2000. (VDI-VDE-Richtlinien). <https://books.google.com.br/books?id=mlrmZwEACAAJ>.

PATHAK, K.; BIRK, A.; VASKEVICIUS, N. Plane-based registration of sonar data for underwater 3d mapping. In: IEEE. *Intelligent Robots and Systems (IROS), 2010 IEEE/RSJ International Conference on*. [S.l.], 2010. p. 4880–4885.

PINHOLE Camera. 2017. `https://commons.wikimedia.org/wiki/File:Pinhole-camera.png`. Accessed: 2017-04-05.

QUAN, X.; FRY, E. S. Empirical equation for the index of refraction of seawater. *Applied Optics*, Optical Society of America, v. 34, n. 18, p. 3477–3480, 1995.

RIBAS, D.; RIDAO, P.; NEIRA, J.; TARDOS, J. D. Slam using an imaging sonar for partially structured underwater environments. In: IEEE. *Intelligent Robots and Systems, 2006 IEEE/RSJ International Conference on*. [S.l.], 2006. p. 5040–5045.

ROSENBLUM, L.; KAMGAR-PARSI, B. 3d reconstruction of small underwater objects using high-resolution sonar data. In: IEEE. *Autonomous Underwater Vehicle Technology, 1992. AUV'92., Proceedings of the 1992 Symposium on*. [S.l.], 1992. p. 228–235.

SANTOLARIA, J.; AGUILAR, J.-J.; GUILLOMÃA, D.; CAJAL, C. A crenellated-target-based calibration method for laser triangulation sensors integration in articulated measurement arms. *Robotics and Computer-Integrated Manufacturing*, v. 27, n. 2, p. 282 – 291, 2011. ISSN 0736-5845.

Translational Research â€“ Where Engineering Meets Medicine. <http://www.sciencedirect.com/science/article/pii/S0736584510000876>.

SANTOLARIA, J.; PASTOR, J. J.; BROSED, F. J.; AGUILAR, J. J. A one-step intrinsic and extrinsic calibration method for laser line scanner operation in coordinate measuring machines. *Measurement Science and Technology*, v. 20, n. 4, p. 045107, 2009. <http://stacks.iop.org/0957-0233/20/i=4/a=045107>.

SCAN Station P20. 2017. `http://w3.leica-geosystems.com/downloads123/hds/hds/ScanStation_P20/brochures-datasheet/Leica_ScanStation_P20_DAT_en.pdf`. Accessed: 2017-04-05.

SCHECHNER, Y. Y.; KARPEL, N. Recovery of underwater visibility and structure by polarization analysis. *IEEE Journal of oceanic engineering*, IEEE, v. 30, n. 3, p. 570–587, 2005.

SCOPOS Tailormade Solutions. 2017. `http://www.scopos.no/index.php/en/products/investigator.html`. Accessed: 2017-04-05.

SUBSEA, Deepwater Camera For Underwater Measurements. 2017. `https://www.youtube.com/watch?v=YqyKJCPxi7g`. Accessed: 2017-04-05.

TAO, L.; CASTELLANI, U.; FUSIELLO, A.; MURINO, V. 3d acoustic image segmentation by a ransac-based approach. In: IEEE. *OCEANS 2003. Proceedings*. [S.l.], 2003. v. 2, p. 1098–1101.

TREIBITZ, T.; SCHECHNER, Y. Y.; SINGH, H. Flat refractive geometry. In: *Computer Vision and Pattern Recognition, 2008. CVPR 2008. IEEE Conference on*. [S.l.: s.n.], 2008. p. 1–8. ISSN 1063-6919.

TRUCCO, E.; FISHER, R. B.; FITZGIBBON, A. W. *Direct calibration and data consistency in 3-D laser scanning*. [S.l.]: Department of Artificial Intelligence, University of Edinburgh, 1994.

ULS-500 PRO. 2017. `https://www.2grobotics.com/products/underwater-laser-scanner-uls-500/`. Accessed: 2017-04-05.

WALDRON, D. L.; MULLEN, L. Underwater optical ranging: A hybrid lidar-radar approach. In: IEEE. *OCEANS 2009, MTS/IEEE Biloxi-Marine Technology for Our Future: Global and Local Challenges*. [S.l.], 2009. p. 1–7.

WOZNIAK, B.; DERA, J. *Light absorption in sea water*. [S.l.]: Springer, 2007.

ZHANG, Z. Flexible camera calibration by viewing a plane from unknown orientations. In: IEEE. *Computer Vision, 1999. The Proceedings of the Seventh IEEE International Conference on.* [S.l.], 1999. v. 1, p. 666–673.